Asian Journal of Physical and Chemical Sciences

3(4): 1-36, 2017; Article no.AJOPACS.36980
ISSN: 2456-7779

Turbulent Thermochemical Non-equilibrium Reentry Flows with Magnetic Actuation in 2D – Seven Species

Edisson Sávio de Góes Maciel[1*] and Cláudia Regina de Andrade[2]

[1]Instituto Tecnológico de Aeronáutica (ITA) – Rua Santa Clara, 245 – Caixa Postal: 2029 – 12.243-970 – São José dos Campos, SP, Brazil.
[2]Instituto Tecnológico de Aeronáutica (ITA) – Praça Mal. do Ar Eduardo Gomes, 50 – 12.228-900 – São José dos Campos, SP, Brazil.

Authors' contributions

This work was carried out in collaboration between both authors. Author ESDGM designed the study, performed the statistical analysis, wrote the protocol, wrote the first draft of the manuscript and managed the analyses of the study. Author CRDA managed the literature searches. Both authors read and approved the final manuscript.

Article Information

DOI: 10.9734/AJOPACS/2017/36980
Editor(s):
(1) Hesham Mansour, Physics Department, Faculty of Science, Cairo University, Egypt.
Reviewers:
(1) Heyuan Wang, Liaoning University of Technology, China.
(2) Omar Dario Lopez Mejia, Universidad de los Andes, Colombia.
(3) Krishna Gopal Singha, Karanga Girls' H. S. S., India.
(4) Xinguang Yang, Henan Normal University, China.
Complete Peer review History: http://www.sciencedomain.org/review-history/21729

Original Research Article

Received 25th September 2017
Accepted 28th October 2017
Published 3rd November 2017

ABSTRACT

In this work, a study involving the Maciel scheme to solve the reactive Favre averaged Navier-Stokes equations, coupled with a turbulence model and the Maxwell equations is performed. The Favre averaged Navier-Stokes equations coupled with the Maxwell equations, in conservative and finite volume contexts, employing structured spatial discretization, are studied. Seven species chemical model, based on the work of Blottner, is considered for the numerical experiments. Turbulence is taken into account considering the implementation of five k-ω two-equation turbulence models, based on the works of Coakley 1983; Wilcox; Yoder, Georgiadids and Orkwis; Coakley 1997; and Rumsey, Gatski, Ying and Bertelrud. For the magnetic coupling, the Gaitonde formulation is taken into account. Three integration methods are studied to march the algorithm in

**Corresponding author: E-mail: edissonsavio@yahoo.com.br;*

time. The “hot gas” hypersonic flow along a blunt body is the numerical experiment for comparisons. The results have indicated that the Coakley 1983 model yields the best prediction of the stagnation pressure value, with an error inferior to 10.00%, and the best prediction of the lift aerodynamic coefficient.

Keywords: Favre averaged Navier-Stokes and Maxwell equations; turbulent flow; magnetic fotmulation; hypersonic flow; reentry conditions.

1. INTRODUCTION

Renewed interest in the area of hypersonic flight has brought Computational Fluid Dynamics (CFD) to the forefront of fluid flow research [1]. Many years have seen a quantum leap in advancements made in the areas of computer systems and software which utilize them for problem solving. Sophisticated and accurate numerical algorithms are devised routinely that are capable of handling complex computational problems. Experimental test facilities capable of addressing complicated high-speed flow problems are still scarce because they are too expensive to build and sophisticated measurements techniques appropriate for such problems, such as the non-intrusive laser, are still in the development stage. As a result, CFD has become a vital tool in the flow problem solution.

In high speed flows, any adjustment of chemical composition or thermodynamic equilibrium to a change in local environment requires certain time. This is because the redistribution of chemical species and internal energies require certain number of molecular collisions, and hence a certain characteristic time. Chemical non-equilibrium occurs when the characteristic time for the chemical reactions to reach local equilibrium is of the same order as the characteristic time of the fluid flow. Similarly, thermal non-equilibrium occurs when the characteristic time for translation and various internal energy modes to reach local equilibrium is of the same order as the characteristic time of the fluid flow. Since chemical and thermal changes are the results of collisions between the constituent particles, non-equilibrium effects prevail in high-speed flows in low-density air.

In chemical non-equilibrium flows the mass conservation equation is applied to each of the constituent species in the gas mixture. Therefore, the overall mass conservation equation is replaced by as many species conservation equations as the number of chemical species considered. The assumption of thermal non-equilibrium introduces additional energy conservation equations – one for every additional energy mode. Thus, the number of governing equations for non-equilibrium flow is much bigger compared to those for perfect gas flow. A complete set of governing equations for non-equilibrium flow may be found in [2-3].

The problems of chemical non-equilibrium in the shock layers over vehicles flying at high speeds and high altitudes in the Earth’s atmosphere have been discussed by several investigators [4-7]. Most of the existing computer codes for calculating the non-equilibrium reacting flow use the one-temperature model, which assumes that all of the internal energy modes of the gaseous species are in equilibrium with the translational mode [6-7]. It has been pointed out that such a one-temperature description of the flow leads to a substantial overestimation of the rate of equilibrium because of the elevated vibrational temperature [5]. A three-temperature chemical-kinetic model has been proposed by [8] to describe the relaxation phenomena correctly in such a flight regime. However, the model is quite complex and requires many chemical rate parameters which are not yet known. As a compromise between the three-temperature and the conventional one-temperature model, a two-temperature chemical-kinetic model has been developed [9-10], which is designated herein as the TTv model. The TTv model uses one temperature T to characterize both the translational energy of the atoms and molecules and the rotational energy of the molecules, and another temperature Tv to characterize the vibrational energy of the molecules, translational energy of the electrons, and electronic excitation energy of atoms and molecules. The model has been applied to compute the thermodynamic properties behind a normal shock wave in a flow through a constant-area duct [9-10]. Radiation emission from the non-equilibrium flow has been calculated using the Non-equilibrium Air Radiation (NEQAIR) program [11-12]. The flow and the radiation computations have been packaged into a single computer program, the Shock-Tube Radiation Program (STRAP) [10].

In spite of the advances made in the area of compressible turbulence modeling in recent years, no universal turbulence model, applicable to such complex flow problems has emerged so far. While the model should be accurate it should also be economical to use in conjunction with the governing equations of the fluid flow. Taking these issues into consideration, k-ω two-equation models have been chosen in the present work [13-17]. These models solve differential equations for the turbulent kinetic energy and the vorticity. Additional differential equations for the variances of temperature and species mass fractions have also been included. These variances have been used to model the turbulence-chemistry interactions in the reacting flows studied here.

The effects associated with the interaction of magnetic forces with conducting fluid flows have been profitably employed in several applications related to nuclear and other [18] technologies and are known to be essential in the explanation of astrophysical phenomena. In recent years, however, the study of these interactions has received fresh impetus in the effort to solve the problems of high drag and thermal loads encountered in hypersonic flight. The knowledge that electrical and magnetic forces can have profound influence on hypersonic flow fields is not new [19-20] – note increased shock-standoff and reduced heat transfer rates in hypersonic flows past blunt bodies under the application of appropriate magnetic fields. The recent interest stems, however, from new revelations of a Russian concept vehicle, known as AJAX [21], which made extensive reference to technologies requiring tight coupling between electromagnetic and fluid dynamic phenomena. A magnetogasdynamics (MGD) generator was proposed [22] to extract energy from the incoming air while simultaneously providing more benign flow to combustion components downstream. The extracted energy could then be employed to increase thrust by MGD pumping of the flow exiting the nozzle or to assist in the generation of a plasma for injection of the body. This latter technique is known to not only reduce drag on the body but also to provide thermal protection [23].

In addition to daunting engineering challenges, some of the phenomena supporting the feasibility of an AJAX type vehicle are fraught with controversy (see, for example, [24]). Resolution of these issues will require extensive experimentation as well as simulation. The latter approach requires integration of several disciplines, including fluid dynamics, electromagnetics, chemical kinetics, and molecular physics amongst others. This paper describes a recent effort to integrate the first three of these, within the assumptions that characterize ideal and non-ideal magnetogasdynamics.

In the present work, a study involving the Maciel scheme to solve the reactive Favre averaged Navier-Stokes equations, coupled with a turbulence model and the Maxwell equations is performed. The Favre averaged Navier-Stokes equations coupled with the Maxwell equations, in conservative and finite volume contexts, employing structured spatial discretization, are studied. Turbulence is taken into account considering the implementation of five k-ω two-equation turbulence models, based on the works of [13-17]. For the magnetic formulation, the [25-26] model is implemented. Three integration methods are studied to march the scheme in time. The “hot gas” hypersonic flow around a blunt body, in two-dimensions, is simulated. The convergence process is accelerated to steady state condition through a spatially variable time step procedure, which has proved effective gains in terms of computational acceleration [27-28]. The reactive simulations involve Earth atmosphere chemical model of seven species and eighteen reactions, based on the [29] model. N, O, N_2, O_2, NO, NO^+ and e^- species are used to perform the numerical comparisons. The results have indicated that the [13] turbulence model yields the best prediction of the stagnation pressure value and of the lift aerodynamic coefficient, although the [16-17] turbulence models are more computationally efficient.

2. FAVRE AVERAGE

The Navier-Stokes equations and the equations for energy and species continuity which governs the flows with multiple species undergoing chemical reactions have been used [30,31,32] for the analysis. Details of the present implementation for the seven species chemical model, the specification of the thermodynamic and transport properties, as well the vibrational model are described in [33-34]. Density-weighted averaging [35] is used to derive the turbulent flow equations from the above relations. For a detailed description of the Favre equations, the g’s equations and the modeling are presented in [36]. The interested reader is encouraged to read this paper.

3. FAVRE-AVERAGED NAVIER-STOKES EQUATIONS COUPLED WITH MAXWELL EQUATIONS

The flow is modeled by the Favre-averaged Navier-Stokes equations coupled with the Maxwell equations and the condition of thermochemical non-equilibrium, where the rotational and vibrational contributions are considered, is taken into account. Details of the seven species model implementation are described in [33-34], and the interested reader is encouraged to read these works to become aware of the present study. The reactive Navier-Stokes equations in thermal and chemical non-equilibrium were implemented on conservative and finite volume contexts, in the two-dimensional space. In this case, these equations in integral and conservative forms can be expressed by:

$$\frac{\partial}{\partial t}\int_V Q dV + \int_S \vec{F}\bullet\vec{n}dS = \int_V S_{CV}dV + \int_V G dV\,,$$

$$\text{with: } \vec{F} = \left(E_e - E_v\right)\vec{i} + \left(F_e - F_v\right)\vec{j}\,, \qquad (1)$$

where: Q is the vector of conserved variables, V is the volume of a computational cell, $\vec{F}$ is the complete flux vector, $\vec{n}$ is the unity vector normal to the flux face, S is the flux area, G is the k-ω two-equation model source term, S_{CV} is the chemical and vibrational source term, E_e and F_e are the convective flux vectors or the Euler flux vectors in the x and y directions, respectively, and E_v and F_v are the viscous flux vectors in the x and y directions, respectively. The $\vec{i}$ and $\vec{j}$ unity vectors define the Cartesian coordinate system. Seventeen (17) conservation equations are solved: one of general mass conservation, two of linear momentum conservation, one of total energy, six of species mass conservation, one of the vibrational internal energy of the molecules, two of the k-ω turbulence model, two of the g-equations, and two of the Maxwell equations. Therefore, one of the species is absent of the iterative process. The CFD literature recommends that the species of biggest mass fraction of the gaseous mixture should be omitted, aiming to result in a minor numerical accumulation error. To the present study, in which is chosen a chemical model to the air composed of seven (7) chemical species (N, O, N_2, O_2, NO, NO^+ and e^-) and eighteen chemical reactions to the [29] model, this species can be the N_2 or the O_2. To this work, the N_2 was chosen. The vectors Q, E_e, F_e, E_v, F_v, G and S_{CV} can, hence, be defined as follows:

$$Q = \begin{Bmatrix} \rho \\ \rho u \\ \rho v \\ \rho Z \\ \rho_1 \\ \rho_2 \\ \rho_4 \\ \rho_5 \\ \rho_6 \\ \rho_7 \\ \rho e_V \\ \rho k \\ \rho\omega \\ \rho Q_h \\ \rho Q_s \\ B_x \\ B_y \end{Bmatrix},\ E_e = \begin{Bmatrix} \rho u \\ \rho u^2 + P - R_b B_x^2/\mu_M \\ \rho uv - R_b B_x B_y/\mu_M \\ (\rho Z + P)u - R_b\left(\vec{V}\bullet\vec{B}/\mu_M\right)B_x \\ \rho_1 u \\ \rho_2 u \\ \rho_4 u \\ \rho_5 u \\ \rho_6 u \\ \rho_7 u \\ \rho e_V u \\ \rho k u \\ \rho\omega u \\ \rho Q_h u \\ \rho Q_s u \\ 0 \\ uB_y - vB_x \end{Bmatrix},\ F_e = \begin{Bmatrix} \rho v \\ \rho uv - R_b B_x B_y/\mu_M \\ \rho v^2 + P - R_b B_y^2/\mu_M \\ (\rho Z + P)v - R_b\left(\vec{V}\bullet\vec{B}/\mu_M\right)B_y \\ \rho_1 v \\ \rho_2 v \\ \rho_4 v \\ \rho_5 v \\ \rho_6 v \\ \rho_7 v \\ \rho e_V v \\ \rho k v \\ \rho\omega v \\ \rho Q_h v \\ \rho Q_s v \\ vB_x - uB_y \\ 0 \end{Bmatrix}; \qquad (2)$$

$$E_v = \begin{Bmatrix} 0 \\ (t_{xx} + \tau_{xx})/Re \\ (t_{xy} + \tau_{xy})/Re \\ (f_x - \phi_x)/Re - q_{J,x}/Re_\sigma \\ (-\rho_1 v_{1x} - \theta_{1x})/Re \\ (-\rho_2 v_{2x} - \theta_{2x})/Re \\ (-\rho_4 v_{4x} - \theta_{4x})/Re \\ (-\rho_5 v_{5x} - \theta_{5x})/Re \\ (-\rho_6 v_{6x} - \theta_{6x})/Re \\ (-\rho_7 v_{7x} - \theta_{7x})/Re \\ (q_{v,x} - \phi_{v,x})/Re \\ \alpha_x/Re \\ \beta_x/Re \\ \gamma_x/Re \\ \delta_x/Re \\ 0 \\ \frac{1}{Re_\sigma}\frac{1}{\sigma}\left[\frac{\partial}{\partial x}\left(\frac{B_y}{\mu_M}\right) - \frac{\partial}{\partial y}\left(\frac{B_x}{\mu_M}\right)\right] \end{Bmatrix}, \quad F_v = \begin{Bmatrix} 0 \\ (t_{xy} + \tau_{xy})/Re \\ (t_{yy} + \tau_{yy})/Re \\ (f_y - \phi_y)/Re - q_{J,y}/Re_\sigma \\ (-\rho_1 v_{1y} - \theta_{1y})/Re \\ (-\rho_2 v_{2y} - \theta_{2y})/Re \\ (-\rho_4 v_{4y} - \theta_{4y})/Re \\ (-\rho_5 v_{5y} - \theta_{5y})/Re \\ (-\rho_6 v_{6y} - \theta_{6y})/Re \\ (-\rho_7 v_{7y} - \theta_{7y})/Re \\ (q_{v,y} - \phi_{v,y})/Re \\ \alpha_y/Re \\ \beta_y/Re \\ \gamma_y/Re \\ \delta_y/Re \\ \frac{1}{Re_\sigma}\frac{1}{\sigma}\left[\frac{\partial}{\partial y}\left(\frac{B_x}{\mu_M}\right) - \frac{\partial}{\partial x}\left(\frac{B_y}{\mu_M}\right)\right] \\ 0 \end{Bmatrix}; \tag{3}$$

in which: ρ is the mixture density; u and v are Cartesian components of the velocity vector in the x and y directions, respectively; $\vec{V}$ is the complete flow velocity vector; P is the pressure term considering the magnetic effect; Z is the fluid total energy considering the contribution of the magnetic field;

$$S_{CV} = \begin{Bmatrix} 0 \\ 0 \\ 0 \\ 0 \\ 0 \\ \dot{\omega}_1 \\ \dot{\omega}_2 \\ \dot{\omega}_4 \\ \dot{\omega}_5 \\ \dot{\omega}_6 \\ \dot{\omega}_7 \\ \sum_{s=mol} \rho_s \left(e^*_{v,s} - e_{v,s}\right)/\tau_s + \sum_{s=mol} \dot{\omega}_s e_{v,s} \\ 0 \\ 0 \\ 0 \\ 0 \\ 0 \\ 0 \end{Bmatrix}; \quad G = \begin{Bmatrix} 0 \\ 0 \\ 0 \\ 0 \\ 0 \\ 0 \\ 0 \\ 0 \\ 0 \\ 0 \\ 0 \\ G_k \\ G_\omega \\ \left(\frac{2\mu_T}{Re\, Pr\, d_T}\right)\left[\left(\frac{\partial h}{\partial x}\right)^2 + \left(\frac{\partial h}{\partial y}\right)^2\right] \\ \left(\frac{2\mu_T}{Re\, Sc_T}\right)\left[\left(\frac{\partial c_T}{\partial x}\right)^2 + \left(\frac{\partial c_T}{\partial y}\right)^2\right] + \frac{\Psi}{Re} \\ 0 \\ 0 \end{Bmatrix}; \tag{4}$$

$\vec{B}$ is the complete magnetic field vector; R_b is the magnetic force number or the pressure number; ρ_1, ρ_2, ρ_4, ρ_5, ρ_6 and ρ_7 are densities of the N, O, O_2, NO, NO^+, and e^-, respectively; k is the turbulent kinetic energy; ω is the turbulent vorticity; Q_h is the product of fluctuating enthalpy, $\overline{h''h''}$; Q_s is the sum of the product of fluctuating mass fraction, $\sum_{i=1}^{ns}\overline{c_i''c_i''}$; B_x and B_y are Cartesian components of the magnetic field vector in the x and y directions, respectively; μ_M is the mean magnetic permeability, with the value of $4\pi x10^{-7}$ T·m/A; e_V is the sum of the vibrational energy of the molecules; the τ's are the components of the Reynolds stress tensor; the t's are the components of the viscous stress tensor; f_x and f_y are viscous work and Fourier heat flux functions; $\rho_s v_{sx}$ and $\rho_s v_{sy}$ represent the species diffusion flux, defined by the Fick law; ϕ_x and ϕ_y are the terms of mixture diffusion; $\phi_{v,x}$ and $\phi_{v,y}$ are the terms of molecular diffusion calculated at the vibrational temperature; α_x, α_y, β_x, β_y, γ_x, γ_y, δ_x and δ_y are two-equation turbulence model parameters; θ_{sx} and θ_{sy} are diffusion terms function of the mass fraction gradients; $\dot{\omega}_s$ is the chemical source term of each species equation, defined by the law of mass action; e_v^* is the molecular-vibrational-internal energy calculated with the translational/rotational temperature; τ_s is the translational-vibrational characteristic relaxation time of each molecule; $q_{v,x}$ and $q_{v,y}$ are the vibrational Fourier heat flux components in the x and y directions, respectively; Re is the laminar Reynolds number; $q_{J,x}$ and $q_{J,y}$ are the components of the Joule heat flux vector in the x and y directions, respectively; Re_σ is the magnetic Reynolds number; σ is the electrical conductivity; G_k and G_ω are k-ω source terms; μ_T is the turbulent viscosity or vorticity viscosity; h is the static enthalpy; and c_T is the total mass fraction sum.

The viscous stresses, in N/m^2, are determined, according to a Newtonian fluid model, by:

$$t_{xx} = \left[2\mu_m\,\partial u/\partial x - 2/3\,\mu_m\left(\partial u/\partial x + \partial v/\partial y\right)\right];$$
$$t_{xy} = \mu_m\left(\partial u/\partial y + \partial v/\partial x\right); \quad (5)$$
$$t_{yy} = \left[2\mu_m\left(\partial v/\partial y\right) - 2/3\,\mu_m\left(\partial u/\partial x + \partial v/\partial y\right)\right],$$

where μ_m is the molecular viscosity. The components of the turbulent stress tensor (Reynolds stress tensor) are described by the following expressions:

$$\tau_{xx} = \left[2\mu_T\,\partial u/\partial x - 2/3\,\mu_T\left(\partial u/\partial x + \partial v/\partial y\right)\right] - 2/3\,\mathrm{Re}\,\rho k;$$
$$\tau_{xy} = \mu_T\left(\partial u/\partial y + \partial v/\partial x\right); \quad (6)$$
$$\tau_{yy} = \left[2\mu_T\,\partial v/\partial y - 2/3\,\mu_T\left(\partial u/\partial x + \partial v/\partial y\right)\right] - 2/3\,\mathrm{Re}\,\rho k.$$

Expressions to f_x and f_y are given below:

$$f_x = \left(t_{xx} + \tau_{xx}\right)u + \left(t_{xy} + \tau_{xy}\right)v + q_x + q_{v,x} + k_x; \quad (7)$$

$$f_y = \left(t_{xy} + \tau_{xy}\right)u + \left(t_{yy} + \tau_{yy}\right)v + q_y + q_{v,y} + k_y, \quad (8)$$

where q_x and q_y are the Fourier heat flux components and are given by:

$$q_x = \left(\mu_m/\mathrm{Pr}\,d_L + \mu_T/\mathrm{Pr}\,d_T\right)\partial h/\partial x; \quad (9)$$

$$q_y = \left(\mu_m/\mathrm{Pr}\,d_L + \mu_T/\mathrm{Pr}\,d_T\right)\partial h/\partial y, \quad (10)$$

where Prd_L and Prd_T are the laminar and turbulent Prandtl numbers, respectively. The $q_{v,x}$ and $q_{v,y}$ are the vibrational heat flux components and are given by:

$$q_{v,x} = k_V\,\partial T_V/\partial x; \quad (11)$$

$$q_{v,y} = k_V\,\partial T_V/\partial y, \quad (12)$$

with k_V being the vibrational thermal conductivity and T_V is the vibrational temperature, what characterizes this model as of two temperatures: translational/rotational and vibrational. The last terms in Eqs. (7)-(8) are k_x and k_y and are defined as follows:

$$k_x = \left(\mu_m + \frac{\mu_T}{\sigma_k}\right)\partial k/\partial x; \text{ and } k_y = \left(\mu_m + \frac{\mu_T}{\sigma_k}\right)\partial k/\partial y. \quad (13)$$

The diffusion terms related to the k-ω equations are defined as:

$$\alpha_x = \left(\mu_m + \mu_T/\sigma_k\right)\partial k/\partial x,$$
$$\alpha_y = \left(\mu_m + \mu_T/\sigma_k\right)\partial k/\partial y; \quad (14)$$

$$\beta_x = (\mu_m + \mu_T/\sigma_\omega)\partial\omega/\partial x,$$
$$\beta_y = (\mu_m + \mu_T/\sigma_\omega)\partial\omega/\partial y; \quad (15)$$

$$\gamma_x = (\mu_m/Prd_L + \mu_T/Prd_T)\partial Q_h/\partial x,$$
$$\gamma_y = (\mu_m/Prd_L + \mu_T/Prd_T)\partial Q_h/\partial y; \quad (16)$$

$$\delta_x = (\mu_m/Sc + \mu_T/Sc_T)\partial Q_S/\partial x,$$
$$\delta_y = (\mu_m/Sc + \mu_T/Sc_T)\partial Q_S/\partial y, \quad (17)$$

with Sc and Sc_T the laminar and turbulent Schmidt numbers, with values 0.22 and 1.00, respectively. The terms of species diffusion, defined by the Fick law, to a condition of thermal non-equilibrium, are determined by [37]:

$$\rho_s v_{sx} = -\rho D_s \frac{\partial Y_{MF,s}}{\partial x} \text{ and}$$
$$\rho_s v_{sy} = -\rho D_s \frac{\partial Y_{MF,s}}{\partial y}, \quad (18)$$

with "s" referent to a given species, $Y_{MF,s}$ being the molar fraction of the species, defined as:

$$Y_{MF,s} = \frac{\rho_s/M_s}{\sum_{k=1}^{ns}\rho_k/M_k} \quad (19)$$

and D_s is the species-effective-diffusion coefficient.

The diffusion terms ϕ_x and ϕ_y which appear in the energy equation are defined by [38]:

$$\phi_x = \sum_{s=1}^{ns}\rho_s v_{sx} h_s \text{ and } \phi_y = \sum_{s=1}^{ns}\rho_s v_{sy} h_s, \quad (20)$$

being h_s the specific enthalpy (sensible) of the chemical species "s". The molecular diffusion terms calculated at the vibrational temperature, $\phi_{v,x}$ and $\phi_{v,y}$, which appear in the vibrational-internal-energy equation are defined by [37]:

$$\phi_{v,x} = \sum_{s=mol}\rho_s v_{sx} h_{v,s} \text{ and } \phi_{v,y} = \sum_{s=mol}\rho_s v_{sy} h_{v,s}, \quad (21)$$

with $h_{v,s}$ being the specific enthalpy (sensible) of the chemical species "s" calculated at the vibrational temperature T_V. The sum of Eq. (4), as also those present in Eq. (21), considers only the molecules of the system, namely: N_2, O_2, NO and NO^+. The θ's terms of Eq. (3) are described as,

$$\theta_{sx} = (\mu_m/Sc + \mu_T/Sc_T)\partial c_S/\partial x; \quad (22)$$

$$\theta_{sy} = (\mu_m/Sc + \mu_T/Sc_T)\partial c_S/\partial y. \quad (23)$$

The Z total energy is defined as:

$$Z = c_{v,mix}(T - T_{REF}) + \Delta h^0_{f,mix} + e_V + 0.5(u^2 + v^2) + R_b\frac{B^2}{2\rho\mu_M} \quad (24)$$

with: T_{REF} is the reference temperature, and $\Delta h^0_{f,mix}$ is the mixture formation enthalpy. The pressure term is expressed by:

$$P = p + R_b\frac{B_x^2 + B_y^2}{2\mu_M} = p + R_b\frac{B^2}{2\mu_M}, \quad (25)$$

with p the fluid static pressure. The magnetic force number or pressure number is determined by:

$$R_b = \frac{B_\infty^2}{\rho_\infty V_\infty^2 \mu_{M,\infty}} = \frac{B_{x,\infty}^2 + B_{y,\infty}^2}{\rho_\infty (u_\infty^2 + v_\infty^2)\mu_{M,\infty}}, \quad (26)$$

where B_∞, ρ_∞, V_∞, and $\mu_{M,\infty}$ are freestream flow properties. The laminar Reynolds number is estimated by:

$$Re = \frac{\rho_\infty V_\infty L_{REF}}{\mu_{m,\infty}}, \quad (27)$$

with L_{REF} a characteristic configuration length. The magnetic Reynolds number is calculated by:

$$Re_\sigma = L_{REF} V_\infty \mu_{M,\infty}\sigma_\infty. \quad (28)$$

The components of the Joule heat flux vector, which characterizes the non-ideal formulation, are determined by:

$$q_{J,x} = -R_b\left\{\frac{B_y}{\mu_M\sigma}\left[\frac{\partial}{\partial x}\left(\frac{B_y}{\mu_M}\right) - \frac{\partial}{\partial y}\left(\frac{B_x}{\mu_M}\right)\right]\right\} \text{ and}$$
$$q_{J,y} = -R_b\left\{\frac{B_x}{\mu_M\sigma}\left[\frac{\partial}{\partial y}\left(\frac{B_x}{\mu_M}\right) - \frac{\partial}{\partial x}\left(\frac{B_y}{\mu_M}\right)\right]\right\}. \quad (29)$$

4. TURBULENCE MODELS

Five turbulence models were implemented according to a k-ω and $k^{1/2}$-ω formulations. Two turbulence models due to Coakley were implemented.

4.1 Coakley Turbulence Model – 1983

The [13] model is a $k^{1/2}$-ω one. The turbulent Reynolds number is defined as

$$R = \sqrt{k}N/\nu_M \,, \tag{30}$$

where: N is the normal distance from the wall to the cell under study and ν_M is the cinematic viscosity. The production term of turbulent kinetic energy is given by

$$P = \left[\left(\frac{\partial u}{\partial y}+\frac{\partial v}{\partial x}\right)\frac{\partial u}{\partial y}\right]\Big/ Re. \tag{31}$$

The function χ is defined as

$$\chi = \sqrt{C_\mu P/\omega^2} - 1. \tag{32}$$

The damping function is given by

$$D = \frac{1-e^{-\alpha R}}{1+\beta\chi}. \tag{33}$$

The turbulent viscosity is defined by

$$\mu_T = ReC_\mu D\rho k/\omega, \tag{34}$$

with: C_μ a constant to be defined. According to the [13] model, the G_k and G_ω terms have the following expressions:

$$G_k = P_k + D_k \quad \text{and} \quad G_\omega = P_\omega + D_\omega, \tag{35}$$

where:

$$P_k = \left(\frac{0.5C_\mu DP}{\omega^2}\right)\rho\omega\sqrt{k}/Re;$$

$$D_k = 0.5\left[-\frac{2}{3}\left(\frac{\partial u}{\partial x}+\frac{\partial v}{\partial y}\right)\Big/\omega - 1\right]\rho\omega\sqrt{k}/Re; \tag{36}$$

$$P_\omega = \left(C_1 C_\mu P/\omega^2\right)\rho\omega^2/Re;$$

$$D_\omega = \left[-\frac{2}{3}C_1\left(\frac{\partial u}{\partial x}+\frac{\partial v}{\partial y}\right)\Big/\omega - C_2\right]\rho\omega^2/Re, \tag{37}$$

where $C_1 = 0.405D + 0.045$. The closure coefficients adopted by the [13] model are: $\sigma_k = 1.0$; $\sigma_\omega = 1.3$; $C_\mu = 0.09$; $C_2 = 0.92$; $\beta = 0.5$; $\alpha = 0.0065$; Prd_L = 0.72; Prd_T = 0.9.

4.2 Wilcox Turbulence Model

The turbulent viscosity is expressed in terms of k and ω as:

$$\mu_T = Re\,\rho k/\omega. \tag{38}$$

In this model, the quantities σ_k and σ_ω have the values $1/\sigma^*$ and $1/\sigma$, respectively, where σ^* and σ are model constants. According to the [14] model, the G_k and G_ω terms have the following expressions:

$$G_k = P_k - D_k \quad \text{and} \quad G_\omega = P_\omega - D_\omega, \tag{39}$$

where:

$$P_k = \mu_T\left[\left(\frac{\partial u}{\partial y}+\frac{\partial v}{\partial x}\right)\frac{\partial u}{\partial y}\right]\Big/Re; \quad D_k = \beta^*\rho k\,\omega/Re; \tag{40}$$

$$P_\omega = \left(\frac{\alpha\omega}{k}\right)P_k \quad \text{and} \quad D_\omega = \beta\rho\omega^2/Re, \tag{41}$$

where the closure coefficients adopted for the [14] model are: $\beta^* = 0.09$; $\beta = 3/40$; $\sigma^* = 0.5$; $\sigma = 0.5$; $\alpha = 5/9$; Prd_L = 0.72; Prd_T = 0.9.

4.3 Yoder, Georgiadids and Orkwis Turbulence Model

According to the [15] model, the turbulent Reynolds number is specified by:

$$Re_T = \rho k/(\mu_m\omega). \tag{42}$$

The parameter α* is given by:

$$\alpha^* = \left(\alpha_0^* + Re_T/R_k\right)/\left(1 + Re_T/R_k\right). \tag{43}$$

The turbulent viscosity is specified by:

$$\mu_T = \mathrm{Re}\,\alpha^*\rho k/\omega. \quad (44)$$

The source term denoted by G in the governing equations contains the production and dissipation terms of k and ω. To the [15] model, the G_k and G_ω terms have the following expressions:

$$G_k = P_k - D_k \quad \text{and} \quad G_\omega = P_\omega - D_\omega. \quad (45)$$

To define the production and dissipation terms, it is necessary firstly to define some parameters. The turbulent Mach number is defined as:

$$M_T = \sqrt{2k/a^2}. \quad (46)$$

It is also necessary to specify the function F:

$$F = \mathrm{MAX}\left(M_T^2 - M_{T,0}^2, 0.0\right). \quad (47)$$

The β^* parameter is given by:

$$\beta^* = 0.09\left[5/18 + \left(\mathrm{Re}_T/R_S\right)^4\right]/\left[1 + \left(\mathrm{Re}_T/R_S\right)^4\right]. \quad (48)$$

Finally, the production and dissipation terms of Eq. (45) are given by

$$P_k = \tau_{xy}\frac{\partial u}{\partial y} \text{ and } D_k = \beta^*\rho\omega k\left(1+\xi_k F\right)/\mathrm{Re}; \quad (49)$$

$$P_\omega = \alpha\omega/kP_k \text{ and } D_\omega = \rho\omega^2\left(\beta + \beta^*\xi_\omega F\right)/\mathrm{Re}, \quad (50)$$

with:

$$\alpha = 5/9\left(\alpha_0 + \mathrm{Re}_T/R_\omega\right)\left(1 + \mathrm{Re}_T/R_\omega\right)/\alpha^*. \quad (51)$$

The [15] turbulence model adopts the following closure coefficients: R_s = 8.0, R_k = 6.0, R_ω = 2.7, ξ_k = 1.0, ξ_ω = 0.0, β = 3/40, $M_{T,0}$ = 0.0, α_0 = 0.1, $\alpha_0^* = \beta/3$, $\sigma_k = 2.0$ and $\sigma_\omega = 2.0$.

4.4 Coakley Turbulence Model - 1997

In the [16] turbulence model, the turbulent viscosity is expressed in terms of k and ω as:

$$\mu_T = \mathrm{Re}C_\mu\rho k/\omega. \quad (52)$$

In this model, the quantities σ_k and σ_ω have the values $1/\sigma^*$ and $1/\sigma$, respectively, where σ^* and σ are model constants.

The source term denoted by G in the governing equations contains the production and dissipation terms of k and ω. To the [16] model, the G_k and G_ω terms have the following expressions:

$$G_k = P_k + D_k \quad \text{and} \quad G_\omega = P_\omega + D_\omega. \quad (53)$$

To define the production and dissipation terms, it is necessary to define firstly some parameters. The $S_{i,j}$ gradient is defined as

$$S_{ij} = 0.5\left(\frac{\partial u}{\partial y} + \frac{\partial v}{\partial x}\right). \quad (54)$$

The gradient S is expressed as

$$S = \sqrt{2S_{ij}S_{ij}}. \quad (55)$$

The η parameter is defined as

$$\eta = S/\omega. \quad (56)$$

The divergent and the parameter λ are determined by

$$D = \frac{\partial u}{\partial x} + \frac{\partial v}{\partial y} \text{ and } \lambda = \frac{D}{\omega}. \quad (57)$$

The coefficient α_k and α_ω are defined by

$$\alpha_k = \frac{2}{3}\left(1 + C_\mu\lambda\right) \text{ and } \alpha_\omega = \alpha_k. \quad (58)$$

The terms of production and destruction of kinetic energy are defined as

$$P_k = C_\mu\eta^2\rho\omega k/\mathrm{Re} \quad \text{and}$$
$$D_k = -\left(\alpha_k\lambda + 1\right)\rho\omega k/\mathrm{Re}. \quad (59)$$

In relation to the terms of production and destruction of vorticity, new terms are defined. The characteristic turbulent length is expressed as

$$l = \sqrt{k}/\omega . \quad (60)$$

The coefficients $\theta_{k\omega}$ and θ_{ω} are defined as

$$\theta_{k\omega} = l^2\left(\frac{\partial k}{\partial x}\frac{\partial \omega}{\partial x}+\frac{\partial k}{\partial y}\frac{\partial \omega}{\partial y}\right)\Big/(k\omega) \quad (61)$$

$$\theta_{\omega} = l^2\left(\frac{\partial \omega}{\partial x}\frac{\partial \omega}{\partial x}+\frac{\partial \omega}{\partial y}\frac{\partial \omega}{\partial y}\right)^2\Big/\omega^2 . \quad (62)$$

The turbulent Reynolds number is determined by

$$R_t = \frac{k}{\nu_m \omega} . \quad (63)$$

Some others parameters are given by

$$R = C_{\mu} R_t/R_o ,\ D_v = \mathrm{TANH}(R) ,\ \theta = \frac{\theta_{k\omega}-\theta_{\omega}}{D_v}; \quad (64)$$

$$\Delta\theta = \mathrm{TANH}\left(|\theta|-\theta\right),\ f_{ii} = \frac{1}{\rho\sqrt{k\omega}}(dp/dx),\ f_i = f_{ii}^2; \quad (65)$$

$$\Delta f_i = \mathrm{TANH}\left(\alpha f_i\right),\ \Delta w = 1-\Delta\theta\left(1-D_v^4\right); \quad (66)$$

$$C_1 = 0.675\left(1-\Delta w\right)+\left(0.35+0.25\Delta f_i\right)\Delta w ; \quad (67)$$

$$\sigma_w = (C_2-C_1)\sqrt{C_{\mu}}/\kappa^2 ,$$
$$dw = 2\sigma_w \Delta w C_{\mu}\theta_{k\omega}. \quad (68)$$

Finally, the production and destruction terms of vorticity are defined as

$$P_{\omega} = C_1 C_{\mu}\eta^2\rho\omega^2/\mathrm{Re} \quad \text{and}$$
$$D_{\omega} = \left(-C_1\alpha_{\omega}\lambda - C_2 + dw\right)\rho\omega^2/\mathrm{Re}. \quad (69)$$

The closure coefficients assume the following values: $C_{\mu} = 0.09$, $C_2 = 0.833$, $\alpha = 5.0$, $\sigma_k = 1.0$, $\sigma = 0.5$, $\sigma^* = 0.5$, $\kappa = 0.41$, $R_o = 10.0$, $\mathrm{Pr}d_L = 0.72$ and $\mathrm{Pr}d_T = 0.9$.

4.5 Rumsey, Gatski, Ying and Bertelrud turbulence model

Finally, the k-ω model of [17] is studied. The equilibrium eddy-viscosity term employed in the diffusion terms is given by

$$\mu_T^* = \mathrm{Re}c_{\mu}^*\rho k/\omega , \quad (70)$$

where $c_{\mu}^* = 0.081.$ The explicit nonlinear constitutive equation that is used to close the Reynolds-averaged Navier-Stokes equations is expressed (after regularization) by

$$\rho\tau_{ii} = 2\mu_t\left[S_{ii}-\frac{1}{3}\left(S_{ii}+S_{jj}\right)\right] + \frac{2\mu_t'\alpha_3}{\omega}\left(S_{ii}W_{ij}+S_{ij}W_{jj}+S_{ij}W_{ii}-S_{jj}W_{ij}\right)-\frac{4\mu_t'\alpha_2}{\omega}\left(S_{ij}S_{ii}+S_{ij}S_{jj}-\frac{1}{3}S_{ij}S_{ij}\right)-\frac{2}{3}\rho k/\mathrm{Re}, \quad (71)$$

and

$$\rho\tau_{ij} = 2\mu_t S_{ij}+\frac{2\mu_t'\alpha_3}{\omega}\left(S_{ii}W_{ij}+S_{ij}W_{jj}+S_{ij}W_{ii}-S_{jj}W_{ij}\right), -\frac{4\mu_t'\alpha_2}{\omega}\left(S_{ij}S_{ii}+S_{ij}S_{jj}\right) \quad (72)$$

where

$$S_{ij} = \frac{1}{2}\left(\frac{\partial u_i}{\partial x_j}+\frac{\partial u_j}{\partial x_i}\right) \text{ and } W_{ij} = \frac{1}{2}\left(\frac{\partial u_i}{\partial x_j}-\frac{\partial u_j}{\partial x_i}\right) \quad (73)$$

are the mean-rate-of-strain tensor and the mean-vorticity tensor, respectively. The turbulent viscosity μ_T is

$$\mu_T = \mathrm{Re}c_{\mu}\rho k/\omega . \quad (74)$$

and

$$c_{\mu} = \frac{3(1+\eta^2)+0.2(\eta^6+\zeta^6)}{3+\eta^2+6\eta^2\zeta^2+6\zeta^2+\eta^6+\zeta^6}\alpha_1 ; \quad (75)$$

$$\eta = (\alpha_2/\omega)(S_{ij}S_{ij})^{\frac{1}{2}} \quad \text{and}$$
$$\zeta = (\alpha_3/\omega)(W_{ij}W_{ij})^{\frac{1}{2}}, \quad (76)$$

where:

α_1 = (4/3-C_2)(g/2); α_2 = (2-C_3)(g/2); α_3 = (2-C_4)(g/2); (77)

$$g = \frac{1}{C_1/2+C_5-1} . \quad (78)$$

The constants that govern the pressure-strain correlation model of [17] are C_1 = 6.8, C_2 = 0.36, C_3 = 1.25, C_4 = 0.4 and C_5 = 1.88. The $\mu_T^{'}$ terms considered in Eqs. (71-72) are given by

$$\mu_T^{'} = \mathrm{Re} c_\mu^{'} \rho k / \omega , \tag{79}$$

where

$$c_\mu^{'} = \frac{3(1+\eta^2)}{3+\eta^2+6\eta^2\zeta^2+6\zeta^2+\eta^6+\zeta^6}\alpha_1 . \tag{80}$$

The source term denoted by G in the governing equation contains the production and dissipation terms of k and ω. To the [17] model, the G_k and G_ω terms have the following expressions:

$$G_k = P_k - D_k \quad \text{and} \quad G_\omega = P_\omega - D_\omega , \tag{81}$$

where:

$$P_k = \rho\left(\tau_{xy}\frac{\partial u}{\partial y}\right), \quad D_k = \rho\omega k/\mathrm{Re}\,; \tag{82}$$

$$P_\omega = \psi\rho\omega\left(\tau_{xy}\frac{\partial u}{\partial y}\right)\Big/ k, \text{ and } D_\omega = \beta\rho\omega^2/\mathrm{Re}. \tag{83}$$

The closure coefficients adopted to the [17] model assume the following values: $\beta = 0.83$; $\kappa = 0.41$; $\sigma_k = 1.4$; $\sigma_\omega = 2.2$; $\mathrm{Prd_L}$ = 0.72; $\mathrm{Prd_T}$ = 0.9; $\psi = \beta - \left[\kappa^2/\sigma_\omega\sqrt{c_\mu^*}\right]$.

5. MACIEL CENTERED SCHEME

Maciel centered scheme is obtained by arithmetical average between the flux at the left and right states of the interface. Considering the two-dimensional and structured case, the algorithm is divided in three parts, as recommended by [39], each one corresponding to a characteristic flux. The first part takes into account the dynamic part, which considers the Navier-Stokes equations plus the Maxwell equations and the four equations of the turbulence model, the second one takes into account the chemical part, and the third part takes into account the vibrational part. Hence, the discrete-dynamic-convective flux, which solves the dynamic part, is given by:

$$R^{\mathrm{Dyn}}_{i+1/2,j} = \frac{1}{2}\left[\begin{pmatrix} \rho u \\ \rho u^2 + P - R_b B_x^2/\mu_M \\ \rho uv - R_b B_x B_y/\mu_M \\ (\rho Z + P)u - R_b(\vec{V}\bullet\vec{B}/\mu_M)B_x \\ \rho k u \\ \rho\omega u \\ \rho Q_h u \\ \rho Q_s u \\ 0 \\ uB_y - vB_x \end{pmatrix}_L + \begin{pmatrix} \rho u \\ \rho u^2 + P - R_b B_x^2/\mu_M \\ \rho uv - R_b B_x B_y/\mu_M \\ (\rho Z + P)u - R_b(\vec{V}\bullet\vec{B}/\mu_M)B_x \\ \rho k u \\ \rho\omega u \\ \rho Q_h u \\ \rho Q_s u \\ 0 \\ uB_y - vB_x \end{pmatrix}_R\right] S_x +$$

$$\frac{1}{2}\left[\begin{pmatrix} \rho v \\ \rho uv - R_b B_x B_y/\mu_M \\ \rho v^2 + P - R_b B_y^2/\mu_M \\ (\rho Z + P)v - R_b(\vec{V}\bullet\vec{B}/\mu_M)B_y \\ \rho k v \\ \rho\omega v \\ \rho Q_h v \\ \rho Q_s v \\ vB_x - uB_y \\ 0 \end{pmatrix}_L + \begin{pmatrix} \rho v \\ \rho uv - R_b B_x B_y/\mu_M \\ \rho v^2 + P - R_b B_y^2/\mu_M \\ (\rho Z + P)v - R_b(\vec{V}\bullet\vec{B}/\mu_M)B_y \\ \rho k v \\ \rho\omega v \\ \rho Q_h v \\ \rho Q_s v \\ vB_x - uB_y \\ 0 \end{pmatrix}_R\right] S_y ; \tag{84}$$

the discrete-chemical-convective flux is defined by:

$$R_{i+1/2,j}^{Chem}=\frac{1}{2}\left[\begin{pmatrix}\rho_1 u\\ \rho_2 u\\ \rho_4 u\\ \rho_5 u\\ \rho_6 u\\ \rho_7 u\end{pmatrix}_L+\begin{pmatrix}\rho_1 u\\ \rho_2 u\\ \rho_4 u\\ \rho_5 u\\ \rho_6 u\\ \rho_7 u\end{pmatrix}_R\right]S_x+\frac{1}{2}\left[\begin{pmatrix}\rho_1 v\\ \rho_2 v\\ \rho_4 v\\ \rho_5 v\\ \rho_6 v\\ \rho_7 v\end{pmatrix}_L+\begin{pmatrix}\rho_1 v\\ \rho_2 v\\ \rho_4 v\\ \rho_5 v\\ \rho_6 v\\ \rho_7 v\end{pmatrix}_R\right]S_y; \tag{85}$$

and the discrete-vibrational-convective flux is determined by:

$$R_{i+1/2,j}^{Vib}=\frac{1}{2}\left[\left(\rho e_v u\right)_L+\left(\rho e_v u\right)_R\right]S_x+\frac{1}{2}\left[\left(\rho e_v v\right)_L+\left(\rho e_v v\right)_R\right]S_y. \tag{86}$$

The viscous formulation follows that of [40], which adopts the Green theorem to calculate primitive variable gradients. The viscous vectors are also obtained by arithmetical average between cell (i,j) and its neighbors. As it was done with the convective terms, there is a need to separate the viscous flux in three parts: dynamical viscous flux, chemical viscous flux and vibrational viscous flux. The dynamical part corresponds to:

$$R_{i+1/2,j}^{Dyn}=\frac{1}{2}\left[\begin{pmatrix}0\\ \left(t_{xx}+\tau_{xx}\right)/Re\\ \left(t_{xy}+\tau_{xy}\right)/Re\\ \left(f_x-\phi_x\right)/Re-q_{J,x}/Re_\sigma\\ \alpha_x/Re\\ \beta_x/Re\\ \gamma_x/Re\\ \delta_x/Re\\ 0\\ \frac{1}{Re_\sigma}\frac{1}{\sigma}\left[\frac{\partial}{\partial x}\left(\frac{B_y}{\mu_M}\right)-\frac{\partial}{\partial y}\left(\frac{B_x}{\mu_M}\right)\right]\end{pmatrix}_L+\begin{pmatrix}0\\ \left(t_{xx}+\tau_{xx}\right)/Re\\ \left(t_{xy}+\tau_{xy}\right)/Re\\ \left(f_x-\phi_x\right)/Re-q_{J,x}/Re_\sigma\\ \alpha_x/Re\\ \beta_x/Re\\ \gamma_x/Re\\ \delta_x/Re\\ 0\\ \frac{1}{Re_\sigma}\frac{1}{\sigma}\left[\frac{\partial}{\partial x}\left(\frac{B_y}{\mu_M}\right)-\frac{\partial}{\partial y}\left(\frac{B_x}{\mu_M}\right)\right]\end{pmatrix}_R\right]S_x+$$

$$\frac{1}{2}\left[\begin{pmatrix}0\\ \left(t_{xy}+\tau_{xy}\right)/Re\\ \left(t_{yy}+\tau_{yy}\right)/Re\\ \left(f_y-\phi_y\right)/Re-q_{J,y}/Re_\sigma\\ \alpha_y/Re\\ \beta_y/Re\\ \gamma_y/Re\\ \delta_y/Re\\ \frac{1}{Re_\sigma}\frac{1}{\sigma}\left[\frac{\partial}{\partial y}\left(\frac{B_x}{\mu_M}\right)-\frac{\partial}{\partial x}\left(\frac{B_y}{\mu_M}\right)\right]\\ 0\end{pmatrix}_L+\begin{pmatrix}0\\ \left(t_{xy}+\tau_{xy}\right)/Re\\ \left(t_{yy}+\tau_{yy}\right)/Re\\ \left(f_y-\phi_y\right)/Re-q_{J,y}/Re_\sigma\\ \alpha_y/Re\\ \beta_y/Re\\ \gamma_y/Re\\ \delta_y/Re\\ \frac{1}{Re_\sigma}\frac{1}{\sigma}\left[\frac{\partial}{\partial y}\left(\frac{B_x}{\mu_M}\right)-\frac{\partial}{\partial x}\left(\frac{B_y}{\mu_M}\right)\right]\\ 0\end{pmatrix}_R\right]S_y; \tag{87}$$

To the chemical part one has:

$$R^{Chem}_{i+1/2,j} = \frac{1}{2}\left[\begin{pmatrix} (-\rho_1 v_{1x} - \theta_{1x})/Re \\ (-\rho_2 v_{2x} - \theta_{2x})/Re \\ (-\rho_4 v_{4x} - \theta_{4x})/Re \\ (-\rho_5 v_{5x} - \theta_{5x})/Re \\ (-\rho_6 v_{6x} - \theta_{6x})/Re \\ (-\rho_7 v_{7x} - \theta_{7x})/Re \end{pmatrix}_L + \begin{pmatrix} (-\rho_1 v_{1x} - \theta_{1x})/Re \\ (-\rho_2 v_{2x} - \theta_{2x})/Re \\ (-\rho_4 v_{4x} - \theta_{4x})/Re \\ (-\rho_5 v_{5x} - \theta_{5x})/Re \\ (-\rho_6 v_{6x} - \theta_{6x})/Re \\ (-\rho_7 v_{7x} - \theta_{7x})/Re \end{pmatrix}_R\right] S_x +$$

$$\frac{1}{2}\left[\begin{pmatrix} (-\rho_1 v_{1y} - \theta_{1y})/Re \\ (-\rho_2 v_{2y} - \theta_{2y})/Re \\ (-\rho_4 v_{4y} - \theta_{4y})/Re \\ (-\rho_5 v_{5y} - \theta_{5y})/Re \\ (-\rho_6 v_{6y} - \theta_{6y})/Re \\ (-\rho_7 v_{7y} - \theta_{7y})/Re \end{pmatrix}_L + \begin{pmatrix} (-\rho_1 v_{1y} - \theta_{1y})/Re \\ (-\rho_2 v_{2y} - \theta_{2y})/Re \\ (-\rho_4 v_{4y} - \theta_{4y})/Re \\ (-\rho_5 v_{5y} - \theta_{5y})/Re \\ (-\rho_6 v_{6y} - \theta_{6y})/Re \\ (-\rho_7 v_{7y} - \theta_{7y})/Re \end{pmatrix}_R\right] S_y \quad ; \tag{88}$$

Finally, to the vibrational part:

$$R^{Vib}_{i+1/2,j} = \frac{1}{2}\left[\left(\frac{q_{v,x} - \phi_{v,x}}{Re}\right)_L + \left(\frac{q_{v,x} - \phi_{v,x}}{Re}\right)_R\right] S_x + \frac{1}{2}\left[\left(\frac{q_{v,y} - \phi_{v,y}}{Re}\right)_L + \left(\frac{q_{v,y} - \phi_{v,y}}{Re}\right)_R\right] S_y \,. \tag{89}$$

where $S_{i+1/2,j} = \left[S_x \quad S_y\right]^t_{i+1/2,j}$ defines the normal area vector for the surface (i+½,j). The normal area components S_x and S_y to each flux interface are given in Tab. 1. Fig. 1 exhibits the computational cell adopted for the simulations, as well its respective nodes and flux interfaces.

The resultant ordinary differential equation system can be written as:

$$V_{i,j}\, dQ_{i,j}/dt = -\left(R_{i,j-1/2} + R_{i+1/2,j} + R_{i,j+1/2} + R_{i-1/2,j}\right) = -C_{i,j}, \tag{90}$$

where the cell volume is given by:

$$V_{i,j} = 0.5\left|\left(x_{i,j} - x_{i+1,j}\right)y_{i+1,j+1} + \left(x_{i+1,j} - x_{i+1,j+1}\right)y_{i,j} + \left(x_{i+1,j+1} - x_{i,j}\right)y_{i+1,j}\right| +$$
$$0.5\left|\left(x_{i,j} - x_{i+1,j+1}\right)y_{i,j+1} + \left(x_{i+1,j+1} - x_{i,j+1}\right)y_{i,j} + \left(x_{i,j+1} - x_{i,j}\right)y_{i+1,j+1}\right|. \tag{91}$$

This centered scheme is second order accurate in space, according to a finite difference discretization, and needs an artificial dissipation operator, D, to guarantee stability in presence of shock waves and background instabilities. Considering this operator, Eq. (90) can be rewritten as:

$$dQ_{i,j}/dt = -\left(C_{i,j} - D_{i,j}\right)/V_{i,j}\,, \tag{92}$$

where D has the following structure:

$$D\left(Q_{i,j}\right) = d^{(2)}\left(Q_{i,j}\right) - d^{(4)}\left(Q_{i,j}\right), \tag{93}$$

with:

$$d^{(2)} = 0.5\varepsilon^{(2)}_{i,j-1/2}\left(A_{i,j} + A_{i,j-1}\right)\left(Q_{i,j-1} - Q_{i,j}\right) + 0.5\varepsilon^{(2)}_{i+1/2,j}\left(A_{i,j} + A_{i+1,j}\right)\left(Q_{i+1,j} - Q_{i,j}\right) +$$
$$0.5\varepsilon^{(2)}_{i,j+1/2}\left(A_{i,j} + A_{i,j+1}\right)\left(Q_{i,j+1} - Q_{i,j}\right) + 0.5\varepsilon^{(2)}_{i-1/2,j}\left(A_{i,j} + A_{i-1,j}\right)\left(Q_{i-1,j} - Q_{i,j}\right) \quad (94)$$

named the undivided Laplacian operator, responsible by the numerical stability in presence of shock waves; and

$$d^{(4)} = 0.5\varepsilon^{(4)}_{i,j-1/2}\left(A_{i,j} + A_{i,j-1}\right)\left(\nabla^2 Q_{i,j-1} - \nabla^2 Q_{i,j}\right) +$$
$$0.5\varepsilon^{(4)}_{i+1/2,j}\left(A_{i,j} + A_{i+1,j}\right)\left(\nabla^2 Q_{i+1,j} - \nabla^2 Q_{i,j}\right) +$$
$$0.5\varepsilon^{(4)}_{i,j+1/2}\left(A_{i,j} + A_{i,j+1}\right)\left(\nabla^2 Q_{i,j+1} - \nabla^2 Q_{i,j}\right) +$$
$$0.5\varepsilon^{(4)}_{i-1/2,j}\left(A_{i,j} + A_{i-1,j}\right)\left(\nabla^2 Q_{i-1,j} - \nabla^2 Q_{i,j}\right), \quad (95)$$

named the bi-harmonic operator, responsible by the background stability (odd-even instabilities, for instance). In this last term,

$$\nabla^2 Q_{i,j} = \left(Q_{i,j-1} - Q_{i,j}\right) + \left(Q_{i+1,j} - Q_{i,j}\right) + \left(Q_{i,j+1} - Q_{i,j}\right) + \left(Q_{i-1,j} - Q_{i,j}\right). \quad (96)$$

In the $d^{(4)}$ operator, $\nabla^2 Q_{i,j}$ is extrapolated from its neighbor cell every time that such one represents an especial boundary layer cell, recognized in the CFD literature as "ghost" cell. The ε terms are defined, for instance, as:

$$\varepsilon^{(2)}_{i,j-1/2} = K^{(2)} MAX\left(\nu_{i,j}, \nu_{i,j-1}\right) \quad \text{and} \quad \varepsilon^{(4)}_{i,j-1/2} = MAX\left[0, \left(K^{(4)} - \varepsilon^{(2)}_{i,j-1/2}\right)\right], \quad (97)$$

in which:

$$\nu_{i,j} = \left(\left|p_{i,j-1} - p_{i,j}\right| + \left|p_{i+1,j} - p_{i,j}\right| + \left|p_{i,j+1} - p_{i,j}\right| + \left|p_{i-1,j} - p_{i,j}\right|\right) \Big/ \left(p_{i,j-1} + p_{i+1,j} + p_{i,j+1} + p_{i-1,j} + 4p_{i,j}\right). \quad (98)$$

represents a pressure sensor employed to identify regions of high gradients. Each time that a neighbor cell represent a ghost cell, it is assumed that, for instance, $\nu_{ghost} = \nu_{i,j}$. The $A_{i,j}$ terms define the particular artificial dissipation operator. Two models were studied in the current work:

(a) Artificial dissipation operator of Mavriplis / Scalar, non-linear, and isotropic model:

In this case, the $A_{i,j}$ terms represent the sum of the contributions of the maximum normal eigenvalue associated to the flux interface of the Euler equations, integrated along each cell face. Based on [41] work, these terms are defined as:

$$A_{i,j} = \left[\left|u_{int}S_x + v_{int}S_y\right|_{i,j-1/2} + a_{int}\left(S_x^2 + S_y^2\right)^{0.5}_{i,j-1/2}\right] + \left[\left|u_{int}S_x + v_{int}S_y\right|_{i+1/2,j} + a_{int}\left(S_x^2 + S_y^2\right)^{0.5}_{i+1/2,j}\right] +$$
$$\left[\left|u_{int}S_x + v_{int}S_y\right|_{i,j+1/2} + a_{int}\left(S_x^2 + S_y^2\right)^{0.5}_{i,j+1/2}\right] + \left[\left|u_{int}S_x + v_{int}S_y\right|_{i-1/2,j} + a_{int}\left(S_x^2 + S_y^2\right)^{0.5}_{i-1/2,j}\right], \quad (99)$$

where "a" represents the sound speed and the interface properties are evaluated by arithmetical average. The $K^{(2)}$ and $K^{(4)}$ constants have typical values of 1/4 and 3/256, respectively.

(b) Artificial dissipation model of Turkel and Vatsa / Scalar, non-linear, and anisotropic model:

The aforementioned artificial dissipation model presents the characteristic of being isotropic. In words, the dissipation introduced artificially in a given coordinate direction to stabilize the scheme weights equally the phenomena originated from all directions, having not a more significant weighting from the particular direction under study. The dissipation is clearly isotropic. The scalar, non-linear and anisotropic artificial dissipation model of [42] aims to provide a numerical attenuation that considers with bigger weight the propagation information effects associated to the characteristic maximum eigenvalue from the coordinate direction under study. Basically, such artificial dissipation model differs from the non-linear, isotropic model of [41] only in the determination of the weighting term of the dissipation operator.

$$A_\xi = \overline{\lambda}_{\xi_{i+1/2,j}}\left[1+\left(\overline{\lambda}_\eta \Big/ \overline{\lambda}_\xi\right)^{0.5}_{i+1/2,j}\right],\ \overline{\lambda}_{\xi_{i+1/2,j}} = \left(\left|un_x + vn_y\right| + a\right)_{i+1/2,j} S_{i+1/2,j} \text{ and } \overline{\lambda}_{\eta_{i+1/2,j}} = \left(\left|un_x + vn_y\right| + a\right)_{i+1/2,j} S_{i+1/2,j}; \tag{100}$$

$$A_\eta = \overline{\lambda}_{\eta_{i,j+1/2}}\left[1+\left(\overline{\lambda}_\xi \Big/ \overline{\lambda}_\eta\right)^{0.5}_{i,j+1/2}\right],\ \overline{\lambda}_{\xi_{i,j+1/2}} = \left(\left|un_x + vn_y\right| + a\right)_{i,j+1/2} S_{i,j+1/2} \text{ and } \overline{\lambda}_{\eta_{i,j+1/2}} = \left(\left|un_x + vn_y\right| + a\right)_{i,j+1/2} S_{i,j+1/2}. \tag{101}$$

To this artificial dissipation model, the recommended values of $K^{(2)}$ and $K^{(4)}$ by [42] are 1/2 and 1/64, respectively.

6. TIME INTEGRATION

Three methods of time integration were studied herein, namely: Euler Backward, Middle Point, and Runge-Kutta 4th Order.

6.1 Euler Backward

This method is first-order accurate in time, to the three types of complete flux. To the convective dynamic component, this method can be represented in general form by:

$$Q_{i,j}^{(n+1)} = Q_{i,j}^{(n)} - \left(\Delta t_{i,j}/V_{i,j}\right)\times\left[C\left(Q_{i,j}^{(n)}\right) - D\left(Q_{i,j}^{(n)}\right)\right], \tag{102}$$

to the convective chemical component, it can be represented in general form by:

$$Q_{i,j}^{(n+1)} = Q_{i,j}^{(n)} - \Delta t_{i,j}\times\left\{\left[C\left(Q_{i,j}^{(n)}\right) - D\left(Q_{i,j}^{(n)}\right)\right]/V_{i,j} - S_C\left(Q_{i,j}^{(n)}\right)\right\}, \tag{103}$$

where the chemical source term S_C is calculated with the temperature T_{rrc} (reaction rate controlling temperature, see [33-34]). Finally, to the convective vibrational component:

$$Q_{i,j}^{(n+1)} = Q_{i,j}^{(n)} - \Delta t_{i,j}\times\left\{\left[C\left(Q_{i,j}^{(n)}\right) - D\left(Q_{i,j}^{(n)}\right)\right]/V_{i,j} - S_V\left(Q_{i,j}^{(n)}\right)\right\}, \tag{104}$$

in which:

$$S_V = \sum_{s=mol} q_{T-V,s} + \sum_{s=mol} S_{C,s} e_{v,s}, \tag{105}$$

where q_{T-V} is the heat flux due to translational-vibrational relaxation, defined in [33-34].

6.2 Middle Point

This method is a second-order, two-stage Runge-Kutta one, to the three types of complete flux. To the convective dynamic component, this method can be represented in general form by:

$$\begin{aligned} Q_{i,j}^{(0)} &= Q_{i,j}^{n} \\ Q_{i,j}^{(k)} &= Q_{i,j}^{(0)} + \alpha_k\left(\Delta t_{i,j}/V_{i,j}\right)\left[C(Q_{i,j}^{(k-1)}) - D(Q_{i,j}^{(k-1)})\right], \\ Q_{i,j}^{n+1} &= Q_{i,j}^{(k)} \end{aligned} \tag{106}$$

to the convective chemical component, it can be represented in general form by:

$$\begin{aligned} Q_{i,j}^{(0)} &= Q_{i,j}^{n} \\ Q_{i,j}^{(k)} &= Q_{i,j}^{(0)} + \alpha_k \Delta t_{i,j}\left\{\left[C(Q_{i,j}^{(k-1)}) - D(Q_{i,j}^{(k-1)})\right]/V_{i,j} - S_C\left(Q_{i,j}^{k-1}\right)\right\}, \\ Q_{i,j}^{n+1} &= Q_{i,j}^{(k)} \end{aligned} \tag{107}$$

and to the convective vibrational component:

$$\begin{aligned} Q_{i,j}^{(0)} &= Q_{i,j}^{n} \\ Q_{i,j}^{(k)} &= Q_{i,j}^{(0)} + \alpha_k \Delta t_{i,j}\left\{\left[C(Q_{i,j}^{(k-1)}) - D(Q_{i,j}^{(k-1)})\right]/V_{i,j} - S_V\left(Q_{i,j}^{k-1}\right)\right\}, \\ Q_{i,j}^{n+1} &= Q_{i,j}^{(k)} \end{aligned} \tag{108}$$

where the α values of each stage are: α_1 = 1/2 and α_2 = 1.0.

6.3 Runge-Kutta 4th Order

This method is a fourth-order, four-stage Runge-Kutta one, to the three types of complete flux. To the convective dynamic component, this method can be represented in general form by:

$$\begin{aligned} Q_{i,j}^{(0)} &= Q_{i,j}^{n} \\ Q_{i,j}^{(k)} &= Q_{i,j}^{(0)} + \alpha_k K_k^{RK}\left(Q_{i,j}^{(k-1)}\right), \\ Q_{i,j}^{n+1} &= Q_{i,j}^{(k)} \end{aligned} \qquad (109)$$

where

$$K_k^{RK}(Q_{i,j}^{(k-1)}) = \left(\Delta t_{i,j}/V_{i,j}\right)\left[C(Q_{i,j}^{(k-1)}) - D(Q_{i,j}^{(k-1)})\right],$$

for k ≤ 3, and for k = 4 one has:

$$Q_{i,j}^{(k)} = Q_{i,j}^{(0)} + \alpha_k\left(K_{k-3}^{RK} + 2K_{k-2}^{RK} + 2K_{k-1}^{RK} + K_k^{RK}\right), \qquad (110)$$

with the α values for each stage being: α_1 = 1/2, α_2 = 1/2, α_3 = 1.0, and α_4 = 1/6. For the convective chemical component, the unique difference is in the definition of K_k^{RK}:

$$K_k^{RK}(Q_{i,j}^{(k-1)}) = \Delta t_{i,j}\left\{\left[C(Q_{i,j}^{(k-1)}) - D(Q_{i,j}^{(k-1)})\right]/V_{i,j} - S_C(Q_{i,j}^{(k-1)})\right\}, \qquad (111)$$

and for the convective vibrational component:

$$K_k^{RK}(Q_{i,j}^{(k-1)}) = \Delta t_{i,j}\left\{\left[C(Q_{i,j}^{(k-1)}) - D(Q_{i,j}^{(k-1)})\right]/V_{i,j} - S_V(Q_{i,j}^{(k-1)})\right\}. \qquad (112)$$

7. SPATIALLY VARIABLE TIME STEP

The spatially variable time step has proved efficient gains in terms of convergence acceleration, as verified by [27-28]. Initially, the parameter σ is determined, where:

$$\sigma_s = \frac{c_s}{M_s} \quad \text{and} \quad \sigma = \sum_{s=1}^{N}\sigma_s, \qquad (113)$$

with c_s being the mass fraction and M_s the molecular weight. The total specific heat at constant volume due to translation is defined as:

$$c_{V,T} = \sum_{s=1}^{N}\sigma_s c_{V,T,s}, \qquad (114)$$

where, for each gas constituent of the seven (7) species chemical model, the specific heat at constant volume, based on the kinetic theory of gases [43], is defined by

$$\begin{aligned} &c_{V,T,N} = \frac{3}{2}R_N,\ c_{V,T,O} = \frac{3}{2}R_O; \\ &c_{V,T,N_2} = \frac{5}{2}R_{N_2},\ c_{V,T,O_2} = \frac{5}{2}R_{O_2}; \\ &c_{V,T,NO} = \frac{5}{2}R_{NO}; \\ &c_{V,T,NO^+} = \frac{5}{2}R_{NO^+} \quad \text{and} \quad c_{V,T,e^-} = \frac{3}{2}R_{e^-}, \end{aligned} \qquad (115)$$

being R_s the specific gas constant. The total pressure of the gaseous mixture is determined by Dalton law, which indicates that the total pressure of the gas is the sum of the partial pressure of each constituent gas, resulting in:

$$p_s = c_s\rho R_s T \quad \text{and} \quad p = \sum_{s=1}^{N} p_s. \qquad (116)$$

The speed of sound to a reactive mixture considering the two-equation turbulence models can be determined by:

$$a = \sqrt{\frac{(1+\beta)p}{\rho} - k}, \qquad (117)$$

where $\beta = \frac{R_{univ}\sigma}{c_{V,T}}$, with R_{univ} = 1.987 cal/(g-mol.K). Finally, the spatially variable time step is defined from the CFL definition:

$$\Delta t_{i,j} = \frac{CFL\Delta s_{i,j}}{\sqrt{u_{i,j}^2 + v_{i,j}^2} + a_{i,j}}, \qquad (118)$$

where $\Delta s_{i,j}$ is the characteristic length of each cell (defined between the minimum cell side and

the minimum centroid distance between each cell and its neighbors).

8. DIMENSIONLESS SCALES, INITIAL AND BOUNDARY CONDITIONS

8.1 Dimensionless Scales

The dimensionless scales employed to the reactive equations consisted in: R_s is dimensionless by a_{char}, where $a_{char} = \sqrt{\gamma p_\infty / \rho_\infty}$; c_v is dimensionless by a_{char}; h_s and Δh_s^0 are dimensionless by a_{char}^2; T and T_v, translational/rotational temperature and vibrational temperature, respectively, are dimensionless by a_{char}; ρ_s and ρ are dimensionless by ρ_∞; u and v are dimensionless by a_{char}; μ is dimensionless by μ_∞; D, diffusion coefficient, dimensionless by $a_{char}^2\, dt_{char}$, where dt_{char} is the minimum time step calculated in the computational domain at the first iteration; $\dot{\omega}$ is dimensionless by $\rho_\infty x10^{-3}/dt_{char}$; e_v is dimensionless by a_{char}^2; p is dimensionless by $\rho_\infty a_{char}^2$; τ_s, relaxation time, is dimensionless by dt_{char}. To the Maxwell equations: the B_x and B_y Cartesian components of the magnetic field dimensionless by B_∞; the magnetic permeability of the mean is dimensionless by $\mu_{M,\infty}$; and the electric conductivity is dimensionless by σ_∞.

8.2 Initial Condition

The initial conditions to this problem, for a seven species chemical model, coupled with a turbulence model and suffering the actuation of a magnetic field, are presented in Tab. 2. The Reynolds number is obtained from data of [44].

8.3 Boundary Conditions

The boundary conditions are basically of three types: solid wall, entrance, and exit. These conditions are implemented with the help of ghost cells.

Wall condition. In the viscous case, the non-slip condition is enforced. Therefore, the tangent velocity component of the ghost volume at wall has the same magnitude as the respective velocity component of its real neighbor cell, but opposite signal. In the same way, the normal velocity component of the ghost volume at wall is equal in value, but opposite in signal, to the respective velocity component of its real neighbor cell. It results in:

$$u_g = -u_r \quad \text{and} \quad v_g = -v_r . \tag{119}$$

where "g" indicates ghost cell properties and "r" indicates real cell properties.

The normal pressure gradient of the fluid at the wall is assumed to be equal to zero according to a boundary-layer like condition. The same hypothesis is applied for the normal temperature gradient at the wall, assuming an adiabatic wall.

From the above considerations, density and translational/rotational temperature are extrapolated from the respective values of its real neighbor volume (zero order extrapolation). The total vibrational internal energy is also extrapolated. The turbulent kinetic energy and the turbulent vorticity at the ghost volumes are determined by the following expressions:

$$k_{ghost} = 0.0 \quad \text{and} \quad \omega_{ghost}^2 = \left[\left(38/3\, v_M\right)/\left(\beta d_n^2\right)\right]^2, \tag{120}$$

where β assumes the value 3/40 and d_n is the distance of the first cell to the wall. The Q_h and Q_s variables are fixed by their initial values (see Table 2).

With the mixture species mass fractions and with the values of the respective specific heats at constant volume, it is possible to obtain the mixture specific heat at constant volume. The mixture formation enthalpy is extrapolated from the real cell. The Cartesian components of the induced magnetic field at the wall to the ghost cells are fixed with their initial values. The magnetic permeability is considered constant with its initial value. The mixture total energy to the ghost cell is calculated by:

$$Z_g = Cv_{mixt,g}\left(T_{tr,g} - T_{REF}\right) + \Delta h^0_{mixt,g} + e_{v,a\,\dim,g} + 0.5\left(u_g^2 + v_g^2\right) + R_b\left(B_{x,g}^2 + B_{y,g}^2\right)/\left(2\mu_{M,g}\rho_g\right). \tag{121}$$

To the species density, the non-catalytic condition is imposed, what corresponds to zero order extrapolation from the real cell.

Entrance condition. It is divided in two flow regimes:

(a) Subsonic flow: Seven properties are specified and three extrapolated in the boundary conditions of the dynamic part of the algorithm. This approach is based on information propagation analysis along characteristic directions in the calculation domain [45]. In other words, for subsonic flow, seven characteristics propagate information pointing into the computational domain. Thus seven flow properties must be fixed at the inlet plane. Just three characteristic lines allow information to travel upstream. So, three flow variables must be extrapolated from the interior grid to the inlet boundary. The total energy and the components of the magnetic field were the extrapolated variables from the real neighbor volumes, for the studied problem. Density and velocity components adopted values of the initial flow. The turbulence kinetic energy and the vorticity were fixed with the values of the initial condition. Q_h and Q_s variables are also fixed with the values $10^{-6}\ h^2_{initial}$ and $10^{-3}\ \sum_{i=s}^{N} c^2_{i,initial}$, respectively. To the chemical part, six information propagate upstream because it is assumed that all six equations are conducted by the eigenvalue "$(q_n$-a)". In the subsonic flow, all eigenvalues are negative and the information should be extrapolated. In the same reasoning to the chemical boundary conditions, the vibrational-internal-energy equation is dictated by the "$(q_n$-a)" eigenvalue and, in the subsonic region, its value is negative. Hence, the vibrational internal energy should be extrapolated.

(b) Supersonic flow: In this case no information travels upstream; therefore all variables are fixed with their initial values.

Exit condition. It is also divided in two flow regimes:

(a) Subsonic flow: Three characteristics propagate information outward the computational domain. Hence, the associated variables should be extrapolated from interior information. The characteristic direction associated to the "$(q_{normal}$-a)" velocity should be specified because it points inward to the computational domain [45]. In this case, the ghost volume total energy and the induced magnetic components are specified from its initial value. Density and velocity components are extrapolated. The turbulence kinetic energy and the vorticity are prescribed and receive the following values: $0.01k_{ff}$ and $10u/L_{REF}$, respectively, where $k_{ff} = 0.5u^2$. Q_h and Q_s variables are also fixed with the values $10^{-6}\ h^2_{initial}$ and $10^{-3}\ \sum_{i=s}^{N} c^2_{i,initial}$, respectively. To the chemical part, the eigenvalue "$(q_n$-a)" is again negative and the characteristics are always flowing in to the computational domain. Hence, the six chemical species under study should have their densities fixed by their initial values. In the same reasoning, the internal vibrational energy should have its value prescribed by its initial value due to the eigenvalue "$(q_n$-a)" be negative.

(b) Supersonic flow: All variables are extrapolated from interior grid cells, as no flow information can make its way upstream. In other words, nothing can be fixed.

9. PHYSICAL PROBLEM AND MESHES

Firstly the blunt body problem is studied. The geometry under study is a blunt body with 1.0 m of nose ratio and parallel rectilinear walls. The far field is located at 20.0 times the nose ratio in relation to the configuration nose.

Fig. 2 shows the viscous mesh used to the blunt body physical problem. This mesh is composed of 2,548 rectangular cells and 2,650 nodes. This mesh is equivalent in finite differences to a one of 53x50 points. An exponential stretching of 5.0% in the η direction was used to the viscous simulations. A "O" mesh is taken as the base to construct such mesh. No smoothing is used in this mesh generation process, being this one constructed in Cartesian coordinates.

10. RESULTS

Tests were performed in a Core i7 processor of 2.1GHz and 8.0Gbytes of RAM microcomputer, in a Windows 7.0 environment. Three (3) orders of reduction of the maximum residual in the field were considered to obtain a converged solution. The residual was defined as the value of the discretized conservation equation. In the dynamic part, such definition results in:

$$\text{Residual} = -\Delta t_{i,j} / V_{i,j} \times \left(C_{i,j} - D_{i,j}\right). \qquad (122)$$

The angle of attack was adopted equal to zero. Only the [41] artificial dissipation operator has yielded converged results.

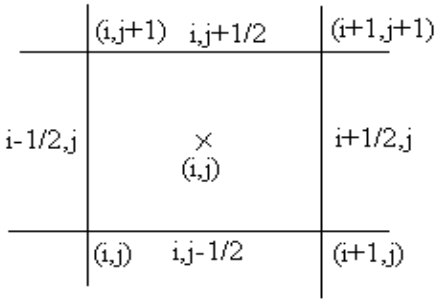

Fig. 1. Computational cell.

10.1 Euler Backward

Coakley (1983) Results. Fig. 3 exhibits the pressure contours obtained by the Maciel scheme as using the [13] turbulence model and the Euler backward method to march in time. Good symmetry properties are observed in these contours. The shock wave is well captured by the Maciel scheme. Fig. 4 shows the turbulent kinetic energy contours obtained as using the [13] turbulence model. Good symmetry properties are observed. The values of k indicate that turbulence is well captured by the numerical algorithm. Fig. 5 presents the B_x magnetic component contours obtained as using the [13] turbulence model. A quantitative symmetrical field is observed as result of the initial condition, which considers only the B_y magnetic component active in this study. Fig. 6 shows the N_2 mass fraction contours obtained in this case. Good N_2 dissociation is observed. Good symmetry properties are also verified.

Wilcox (1988) Results. Fig. 7 exhibits the pressure contours obtained by the Maciel scheme as using the [14] turbulence model and the Euler backward time marching method. Good symmetry properties are observed in the field. Fig. 8 shows the turbulent kinetic energy contours obtained as using the [14] turbulence model. The level of turbulence is bigger than that observed in the [13] turbulence model. Moreover, the k contours captured by the [14] model present worse behavior than the [13] k contours. Fig. 9 presents the B_x magnetic component contours with good symmetry properties as in qualitative as in quantitative aspects. Fig. 10 shows the N_2 mass fraction contours obtained as using the [14] turbulence model. Good dissociation of N_2 is observed, more than that observed with the [13] turbulence model. Good symmetry properties are also verified.

Yoder, Geoirgiadids and Orkwis (1996) Results. Fig. 11 exhibits the pressure contours captured by the Maciel scheme as using the [15] turbulence model and the Euler backward time marching method. The stagnation pressure is inferior to those observed in the [13] and [14] turbulence models. Fig. 12 shows the turbulent kinetic energy contours. They are qualitatively different from those observed in the [13] and [14] turbulence models. However, major turbulence effects in relation to the [13] turbulence results are observed. Fig. 13 presents the B_x magnetic component contours. Good qualitative and quantitative aspects are noted. Fig. 14 shows the N_2 mass fraction contours captured by the Maciel scheme as using the [15] turbulence model. Again, good dissociation and symmetry properties are verified.

Coakley (1997) Results. Fig. 15 exhibits the pressure contours captured by the Maciel scheme as using the [16] turbulence model and the Euler backward time marching method. Good symmetry properties are observed. Fig. 16 shows the turbulent kinetic energy contours and good comparison with the [13] turbulence results are observed. Fig. 17 presents the B_x magnetic component contours and the most intense magnetic field is captured with this turbulence model. Good symmetry properties are observed. Fig. 18 shows the N_2 mass fraction contours generated by the Maciel scheme as using the [16] turbulence model. Good dissociation of N_2 is observed as well good symmetry properties.

Rumsey, Gatski, Ying and Bertelrud (1998) Results. Fig. 19 exhibits the pressure contours captured by the Maciel scheme as using the [17] turbulence model and the Euler backward method is employed to march in time. Good symmetry properties are observed. Fig. 20 shows the turbulent kinetic energy contours captured by the Maciel scheme as using the [17] turbulence model. Good comparison with the [13] and the [16] turbulence models is verified. Good homogeneous and symmetry properties are observed in this figure. Fig. 21 presents the B_x magnetic component contours and little differences are observed in the symmetry properties. Fig. 22 shows the N_2 mass fraction contours obtained by the Maciel scheme as using the [17] turbulence model. Good

dissociation is observed, comparable with the other results.

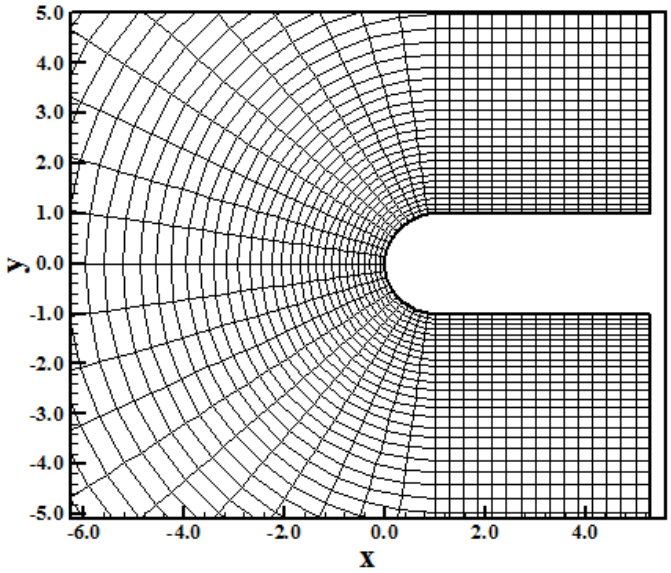

Fig. 2. Blunt body viscous mesh.

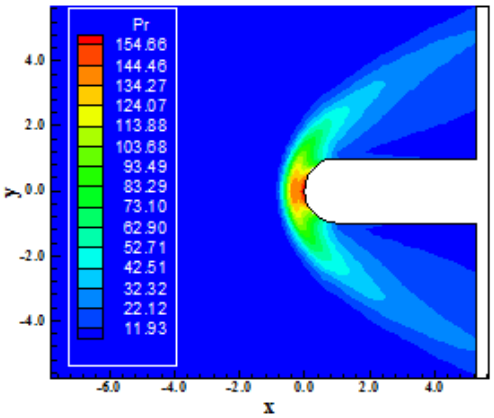

Fig. 3. Pressure contours (EB-C83).

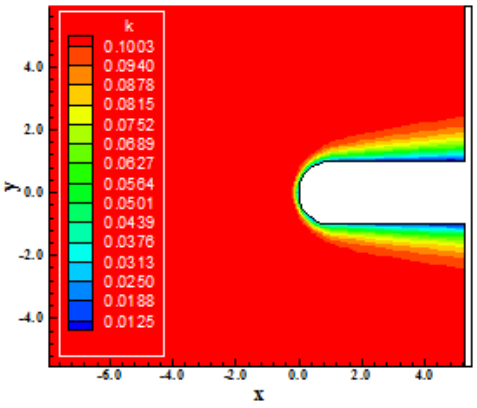

Fig. 4. Turbulent kinetic energy contours (EB-C83).

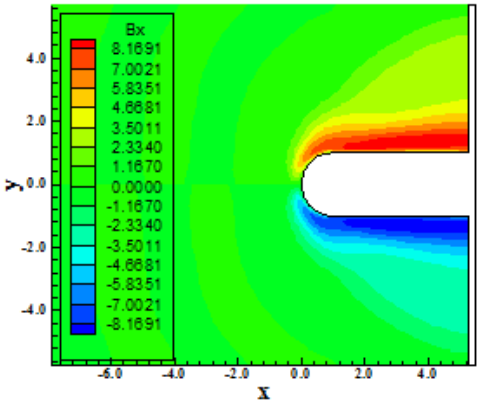

Fig. 5. B_x magnetic component contours (EB-C83).

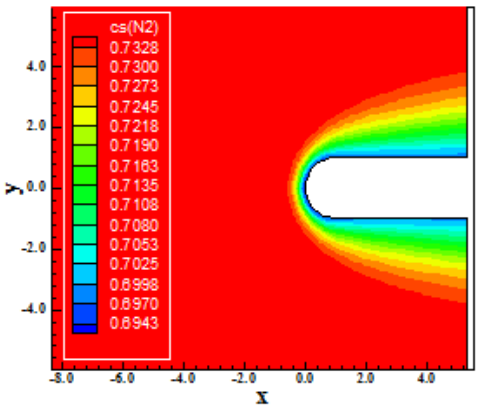

Fig. 6. N_2 mass fraction contours (EB-C83).

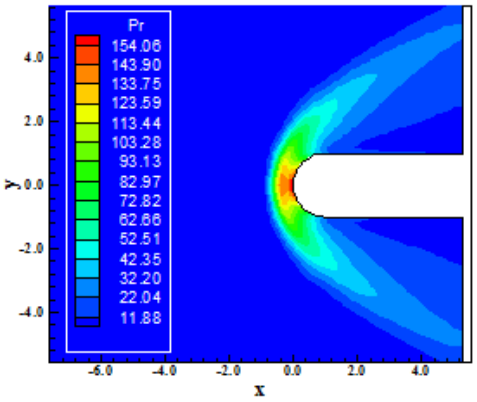

Fig. 7. Pressure contours (EB-W88).

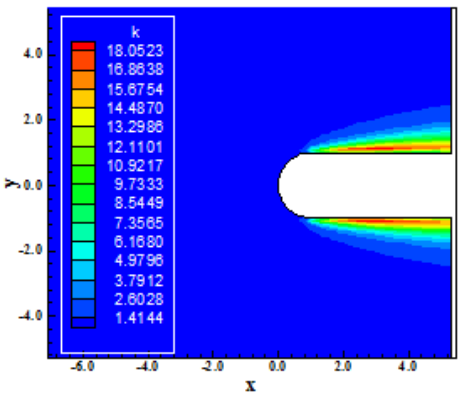

Fig. 8. Turbulent kinetic energy contours (EB-W88).

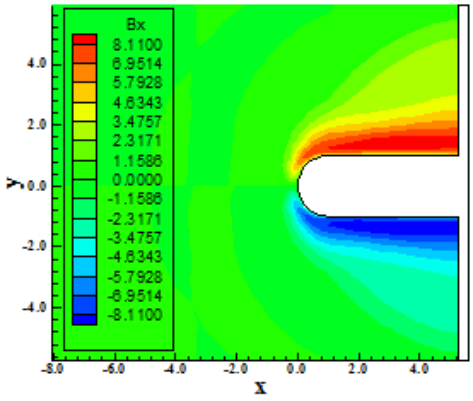

Fig. 9. B_x magnetic component contours (EB-W88).

10.2 Middle Point

Coakley (1983) Results. Fig. 23 exhibits the pressure contours captured by the Maciel scheme as using the [13] turbulence model and the Middle Point time marching method. Good symmetry properties are observed. Fig. 24 shows the turbulent kinetic energy contours obtained by the Maciel scheme as using the [13] turbulence model. Good turbulence effects are observed. Fig. 25 presents the B_x magnetic component contours, where good symmetry properties are observed as in qualitative as in quantitative terms. Fig. 26 shows the N_2 mass fraction contours generated by the Maciel scheme as solution of this reactive-turbulent-magnetic physical problem. Good dissociation of N_2 is perceptible.

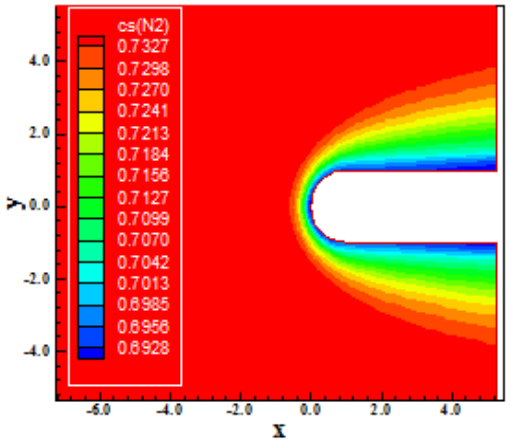

Fig. 10. N_2 mass fraction contours (EB-W88).

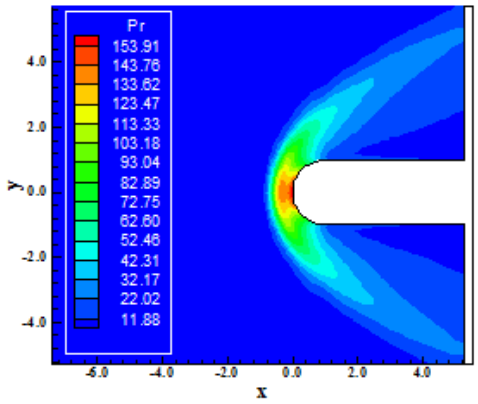

Fig. 11. Pressure contours (EB-YGO86).

Wilcox (1988) Results. Fig. 27 exhibits the pressure contours obtained by the Maciel scheme as using the [14] turbulence model and the Middle Point time marching method. Again, good symmetry properties are observed. Fig. 28 shows the turbulent kinetic energy contours obtained when the [14] turbulence model is employed. Again, bigger levels of turbulence are observed for this turbulence model and its qualitative aspects are worse than the other models. Fig. 29 presents the B_x magnetic component contours obtained by the Maciel scheme as using the [14] turbulence model. Good symmetry properties are observed as in qualitative as in quantitative aspects. Fig. 30 shows the N_2 mass fraction contours generated by the Maciel scheme. Good N_2 dissociation is observed, comparable to that obtained by this model when using the Euler backward method.

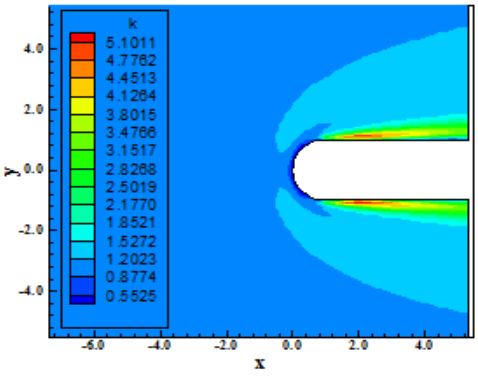

Fig. 12. Turbulent kinetic energy contours (EB-YGO96).

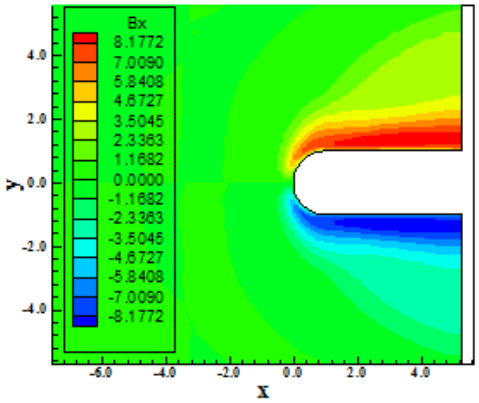

Fig. 13. B_x magnetic component contours (EB-YGO96).

Yoder, Georgiadids and Orkwis (1996) Results. Fig. 31 exhibits the pressure contours captured by the Maciel scheme as using the [15] turbulence model and the Middle Point is employed to march the solution in time. Again, this turbulence model predicts the minor value to the stagnation pressure. Good symmetry properties are observed. Fig. 32 shows the turbulent kinetic energy contours and again the behavior observed in the Euler backward method is repeated here. Bigger levels of turbulence are perceptible in this solution. Fig. 33 presents the B_x magnetic component contours captured by the Maciel scheme as using the [15] turbulence model. Good symmetry properties are observed in quantitative and qualitative terms. Fig. 34 shows the N_2 mass fraction contours generated by the Maciel scheme as using the [15] turbulence model. Again, good dissociation of N_2 is verified. Good symmetry characteristics are also perceptible.

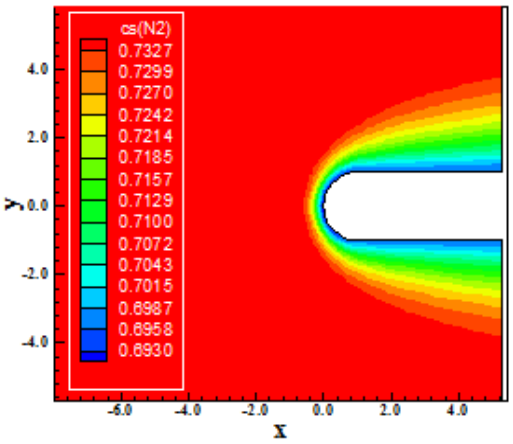

Fig. 14. N_2 mass fraction contours

(EB-YGO96).

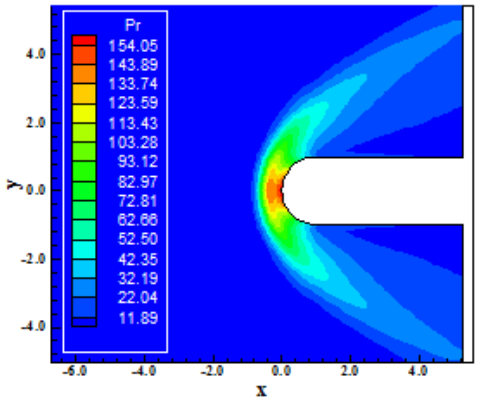

Fig. 15. Pressure contours (EB-C97).

Coakley (1997) Results. Fig. 35 exhibits the pressure contours detected by the Maciel scheme as employing the [16] turbulence model and the time marching method is the Middle Point. Good symmetry properties are observed. Fig. 36 shows the turbulent kinetic energy contours again comparable with the [13] turbulence model. Reasonable levels of turbulence are verified. Good symmetry properties are noted. Fig. 37 presents the B_x magnetic component contours with good qualitative and quantitative aspects. Again, the most severe B_x field is captured with this turbulence model. Fig. 38 shows the N_2 mass fraction contours generated by the Maciel scheme. Good dissociation is observed in this case, with good symmetry properties.

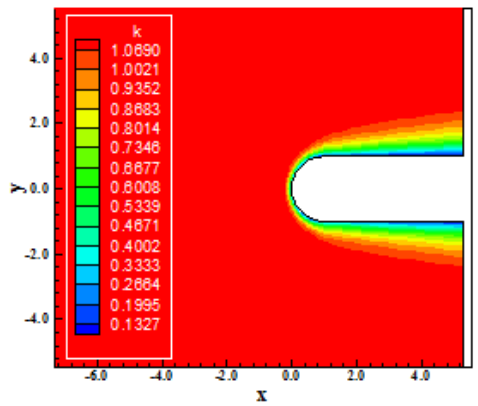

Fig. 16. Turbulent kinetic energy contours (EB-C97).

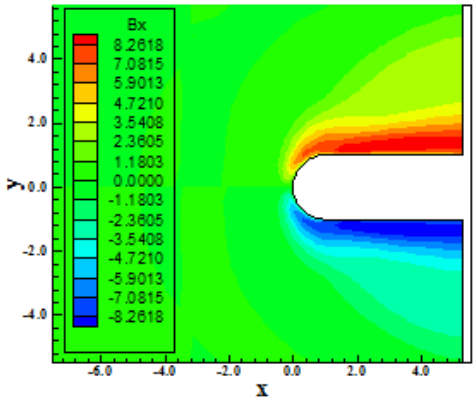

Fig. 17. B_x magnetic component contours (EB-C97).

Rumsey, Gatski, Ying and Bertelrud (1998) Results. Fig. 39 exhibits the pressure contours obtained by the Maciel scheme as using the [17] turbulence model and the Middle Point method to march in time. Good symmetry properties are observed. Fig. 40 shows the turbulent kinetic energy contours generated by the Maciel scheme. These contours are in agreement with the respective contours of the [13] and [16] turbulence models. Fig. 41 presents the B_x magnetic component contours generated by the Maciel scheme as using the [17] model. Discrete differences are observed quantitatively by this turbulence model, but the qualitative aspects are of good resolution. Fig. 42 shows the N_2 mass fraction contours generated by the Maciel scheme. Good symmetry properties are observed with good dissociation levels.

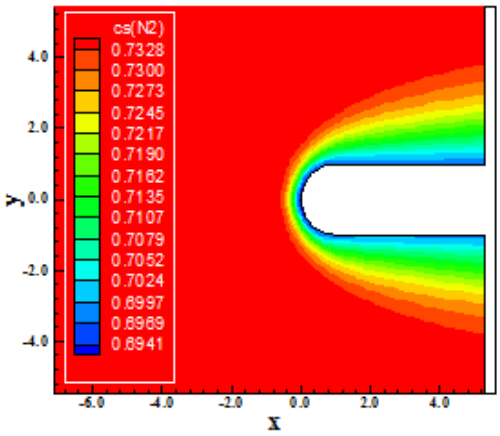

Fig. 18. N_2 mass fraction contours (EB-C97).

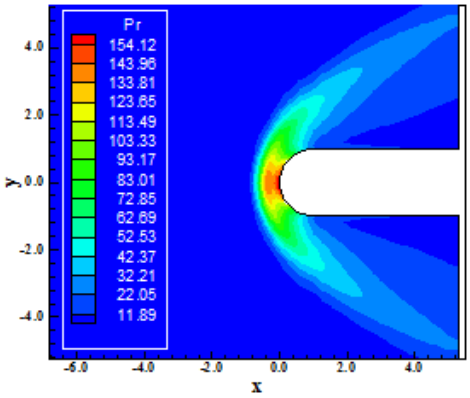

Fig. 19. Pressure contours (EB-RGYB98).

10.3 Runge-Kutta 4th Order

Coakley (1983) Results. Fig. 43 exhibits the pressure contours calculated by the Maciel scheme as using the [13] turbulence model and the Runge-Kutta 4th order method to march in time. Good symmetry properties are observed. Fig. 44 shows the turbulent kinetic energy contours obtained by the Maciel scheme as using the [13] turbulence model. Good levels of turbulence are captured. Fig. 45 presents the B_x magnetic component contours calculated with the Maciel scheme. Good symmetry aspects are observed as in quantitative as in qualitative terms. Fig. 46 shows the N_2 mass fraction contours obtained by the Maciel scheme. Good dissociation and symmetry aspects are observed in this figure.

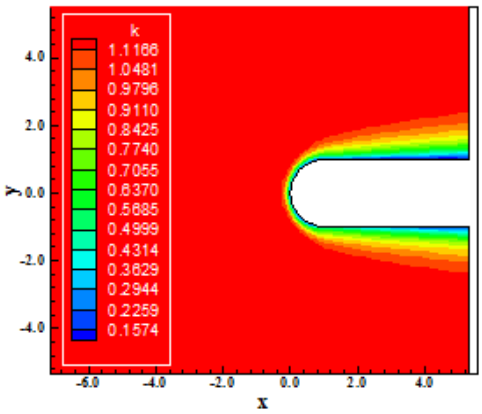

Fig. 20. Turbulent kinetic energy contours (EB-RGYB98).

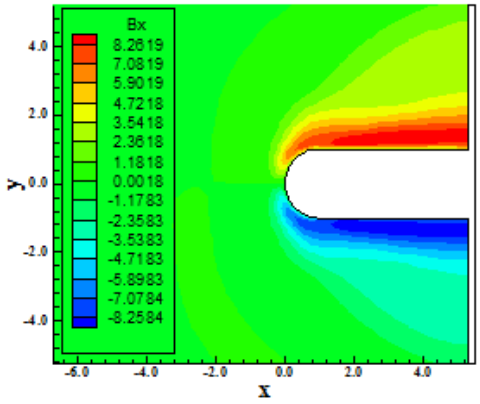

Fig. 21. B_x magnetic component contours (EB-RGYB98).

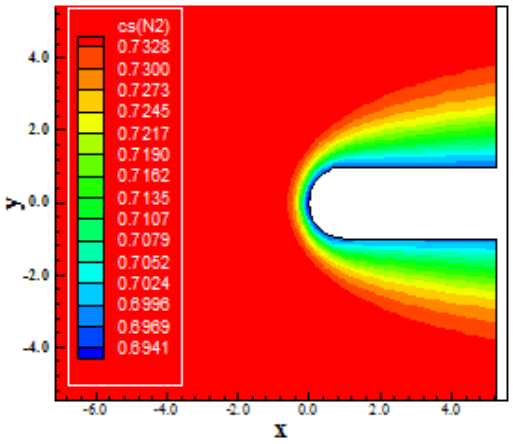

Fig. 22. N_2 mass fraction contours (EB-RGYB98).

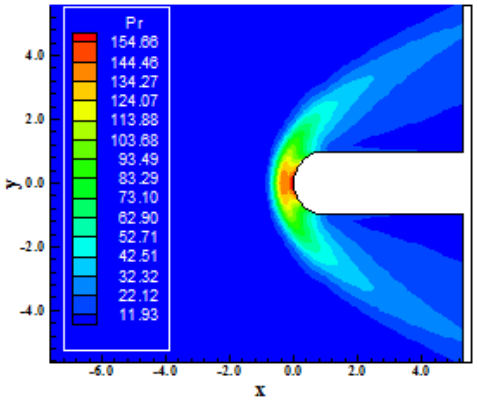

Fig. 23. Pressure contours (MP-C83).

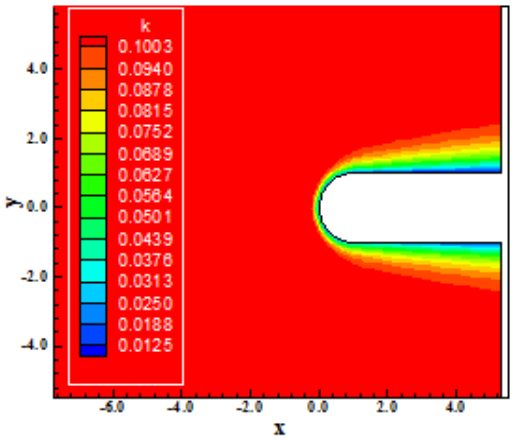

Fig. 24. Turbulent kinetic energy contours (MP-C83).

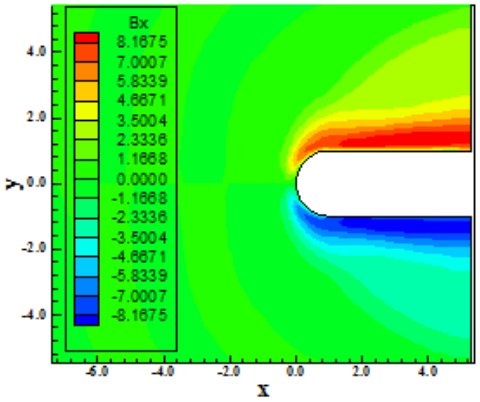

Fig. 25. B_x magnetic component contours (MP-C83).

Wilcox (1988) Results. Fig. 47 exhibits the pressure contours calculated by the Maciel scheme as using the [14] turbulence model and the Runge-Kutta 4th order method to march in time. Good symmetry properties are observed. Fig. 48 shows the turbulent kinetic energy contours obtained by the Maciel scheme as using the [14] turbulence model. High levels of turbulence were captured, with the same problem in qualitative aspects as observed in the previous solutions of this turbulence model. Fig. 49 presents the B_x magnetic component contours captured by the Maciel scheme as using the [14] turbulence model. Good aspects are observed as in quantitative as in qualitative terms. Fig. 50 shows the N_2 mass fraction contours calculated by the Maciel scheme. Good dissociation and symmetry properties are noted.

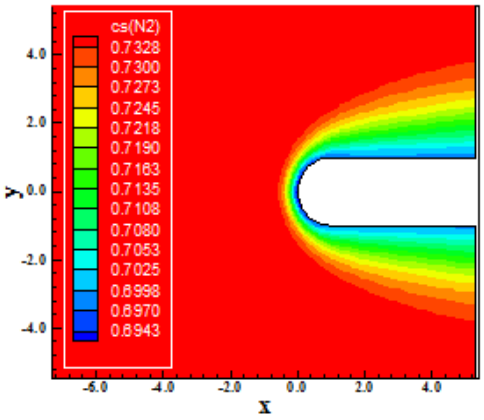

Fig. 26. N_2 mass fraction contours (MP-C83).

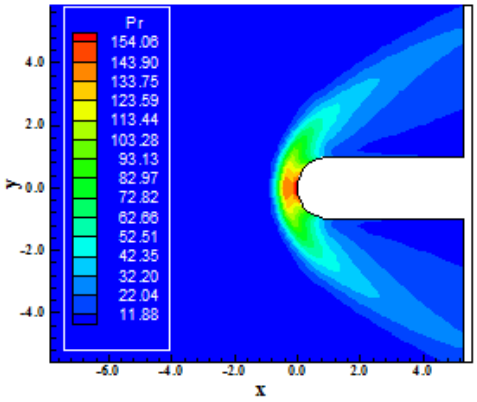

Fig. 27. Pressure contours (MP-W88).

Yoder, Georgiadids and Orkwis (1996) Results. Fig. 51 exhibits the pressure contours calculated with the Maciel scheme as using the [15] turbulence model and the Runge-Kutta 4th order method to march in time. Good symmetry properties are observed. The minimum value to the stagnation pressure is obtained with this turbulence model in all cases studied in this work. Fig. 52 shows the turbulent kinetic energy contours obtained with the Maciel scheme as using the [15] turbulence model. The qualitative aspects are different of all studied cases in this work. High levels of turbulence are obtained. Fig. 53 presents the B_x magnetic component contours obtained by the Maciel scheme as using the [15] turbulence model. Good symmetry aspects are observed qualitatively and quantitatively. Fig. 54 shows the N_2 mass fraction contours obtained by the Maciel scheme as using the [15] turbulence model. Minor dissociation levels are observed in

relation to the other solutions studied herein. Good symmetry aspects are verified.

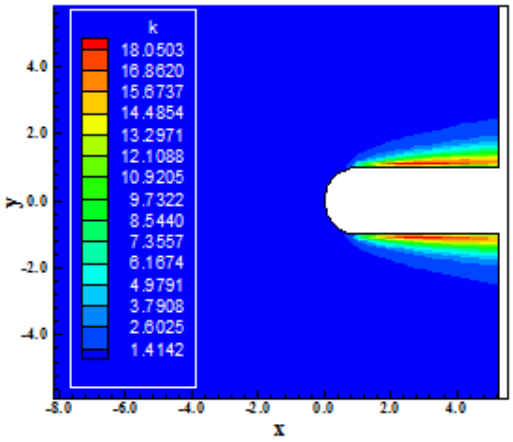

Fig. 28. Turbulent kinetic energy contours (MP-W88).

Coakley (1997) Results. Fig. 55 exhibits the pressure contours calculated by the Maciel scheme as using the [16] turbulence model and the Runge-Kutta 4th order method to march in time. Good symmetry properties are observed. Fig. 56 shows the turbulent kinetic energy contours generated by the Maciel scheme as using the [16] turbulence model. Good comparison with the [13] solutions is verified. Fig. 57 presents the B_x magnetic component contours generated by the Maciel scheme as using the [16] turbulence model. Good symmetry properties are observed. The solution is free of oscillations. Fig. 58 shows the N_2 mass fraction contours obtained by the Maciel scheme as using the [16] turbulence model. Good symmetry properties are noted.

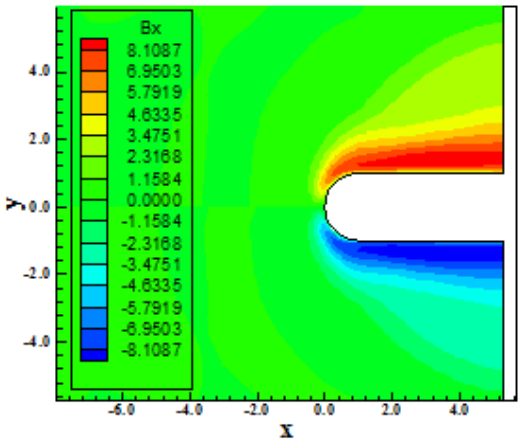

Fig. 29. B_x magnetic component contours (MP-W88).

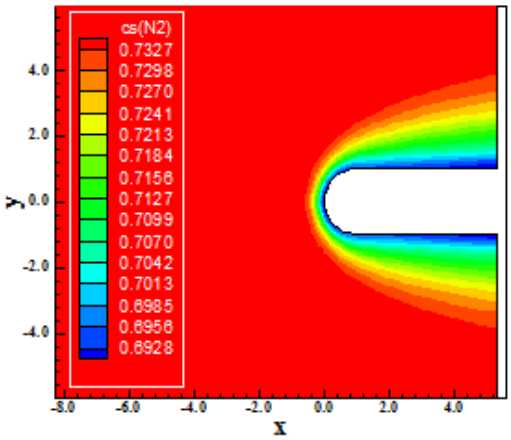

Fig. 30. N_2 mass fraction contours (MP-W88).

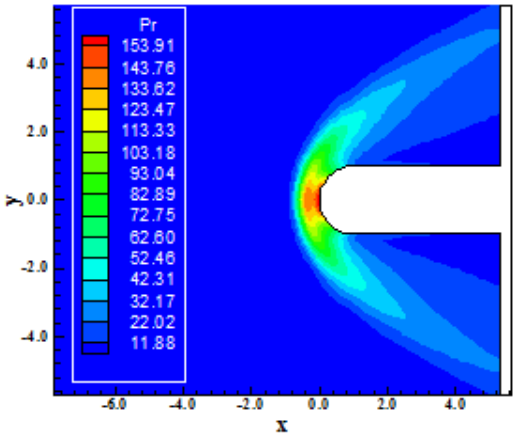

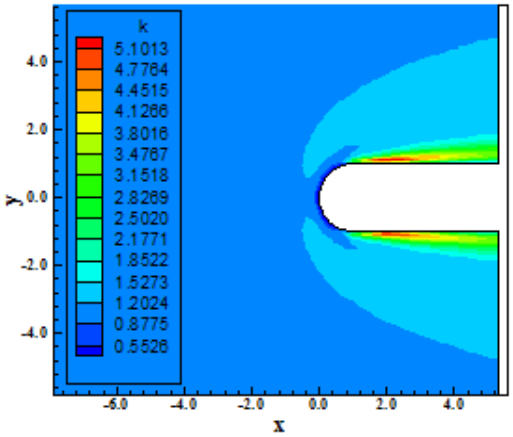

Fig. 32. Turbulent kinetic energy contours

Fig. 31. Pressure contours (MP-YGO96).

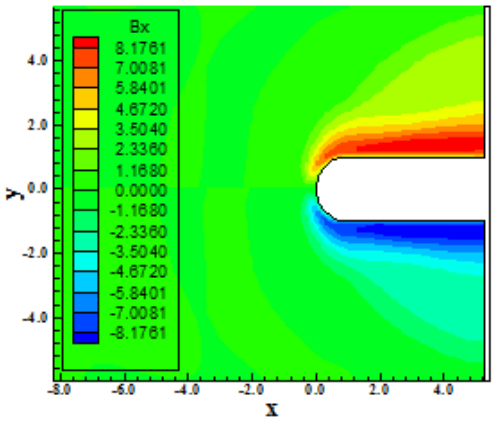

Fig. 33. B_x magnetic component contours (MP-YGO96).

(MP-YGO96).

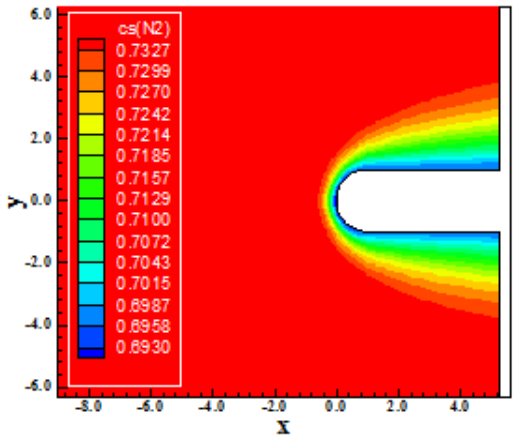

Fig. 34. N_2 mass fraction contours (MP-YGO96).

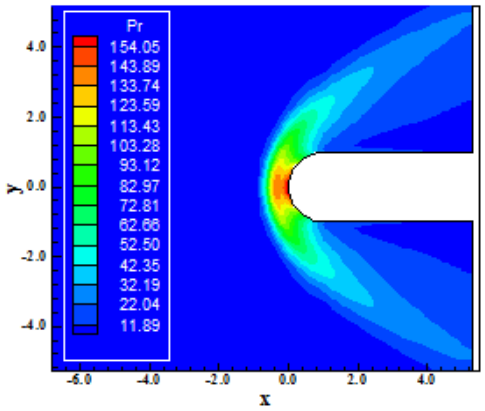

Fig. 35. Pressure contours (MP-C97).

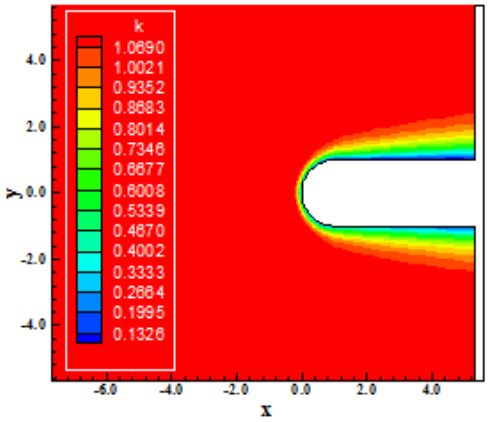

Fig. 36. Turbulent kinetic energy contours (MP-C97).

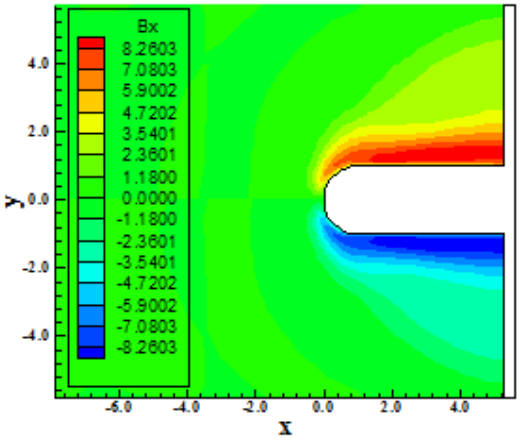

Fig. 37. B_x magnetic component contours (MP-C97).

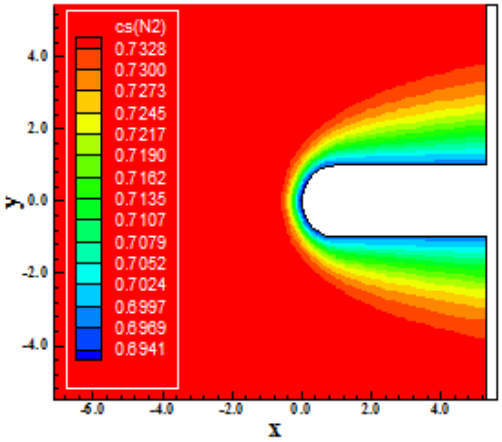

Fig. 38. N_2 mass fraction contours (MP-C97).

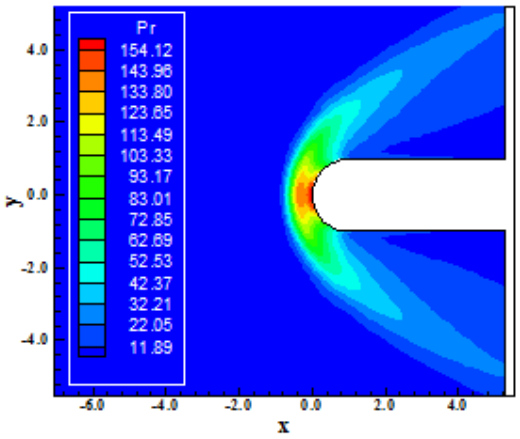

Fig. 39. Pressure contours (MP-RGYB98).

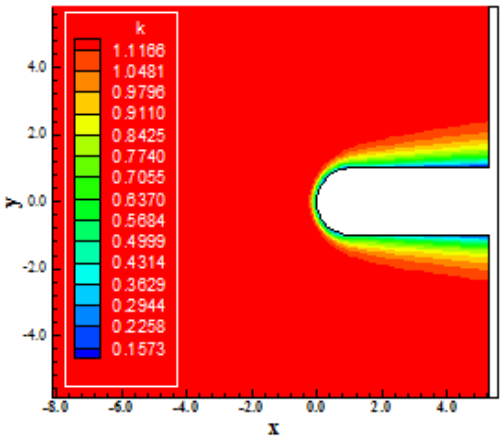

Fig. 40. Turbulent kinetic energy contours (MP-RGYB98).

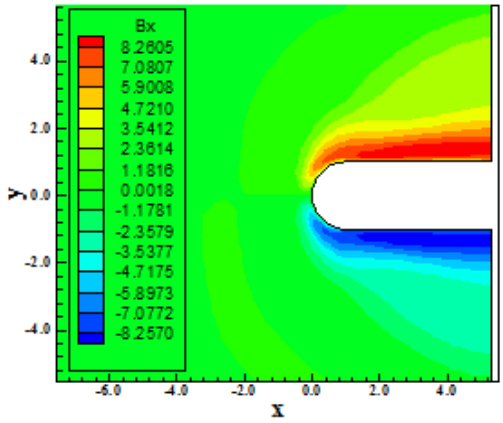

Fig. 41. B_x magnetic component contours (MP-RGYB98).

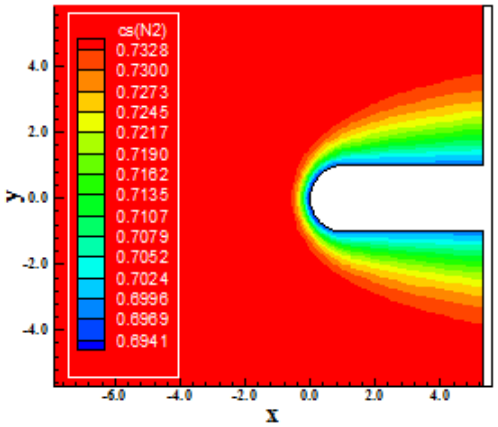

Fig. 42. N_2 mass fraction contours (MP-RGYB98).

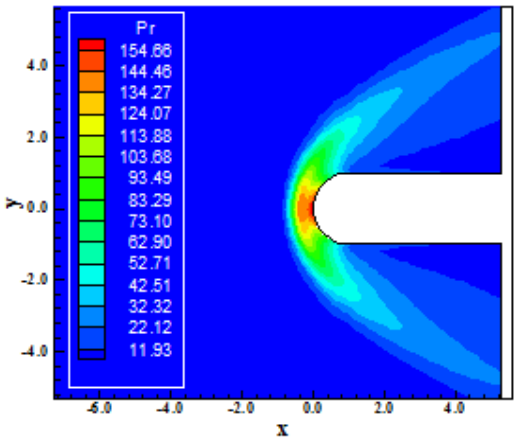

Fig. 43. Pressure contours (RK-C83).

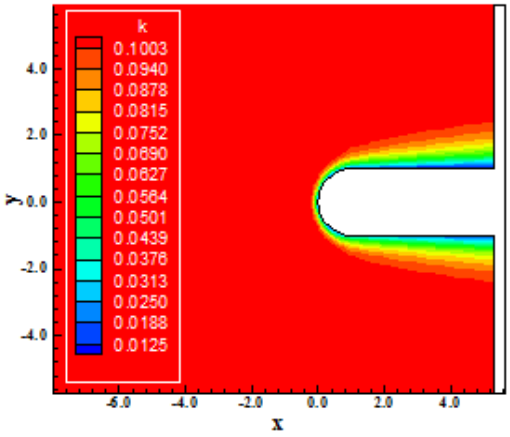

Fig. 44. Turbulent kinetic energy contours (RK-C83).

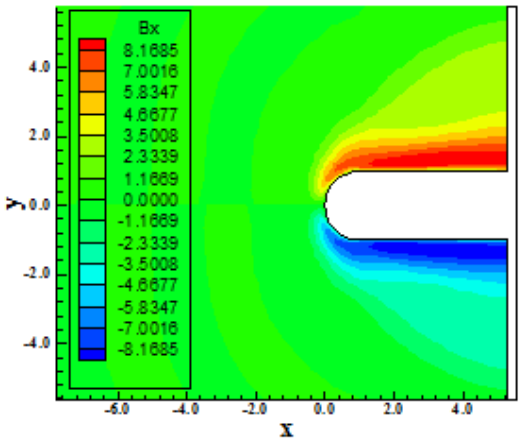

Fig. 45. B_x magnetic component contours (RK-C83).

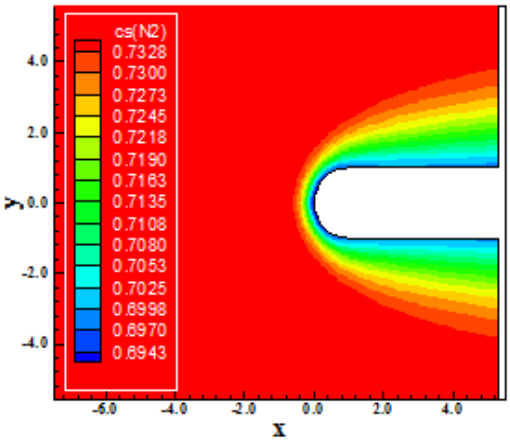

Fig. 46. N_2 mass fraction contours (RK-C83).

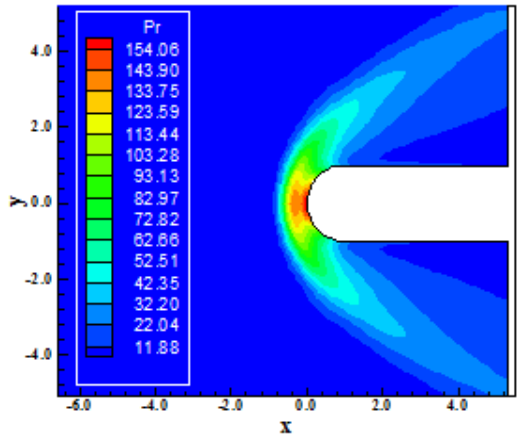

Fig. 47. Pressure contours (RK-W88).

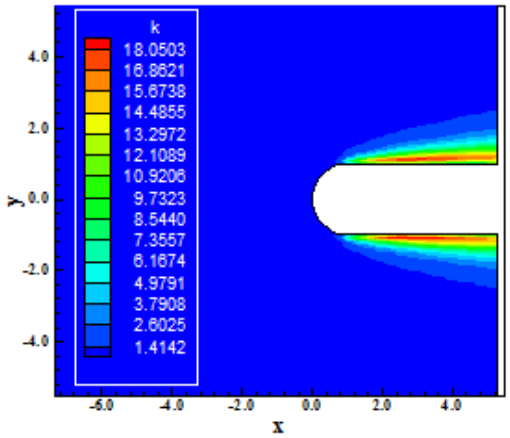

Fig. 48. Turbulent kinetic energy contours (RK-W88).

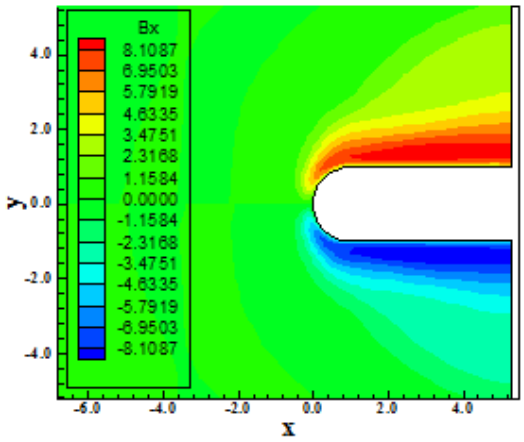

Fig. 49. B_x magnetic component contours (RK-W88).

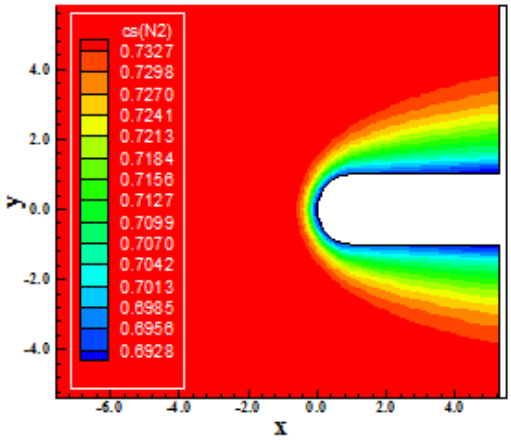

Fig. 50. N_2 mass fraction contours (RK-W88).

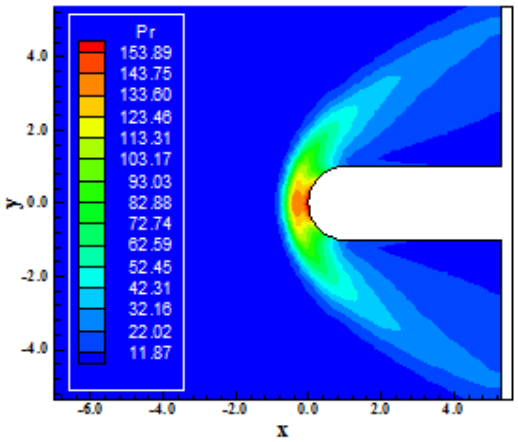

Fig. 51. Pressure contours (RK-YGO96).

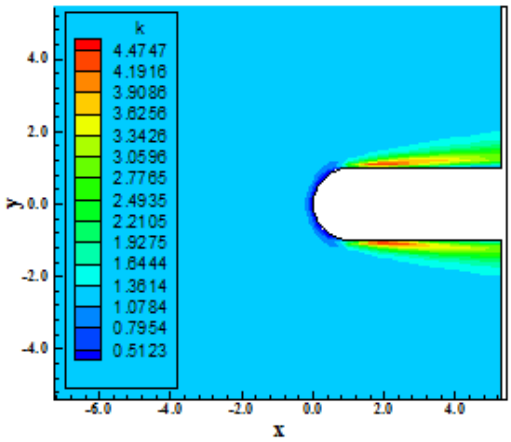

Fig. 52. Turbulent kinetic energy contours (RK-YGO96).

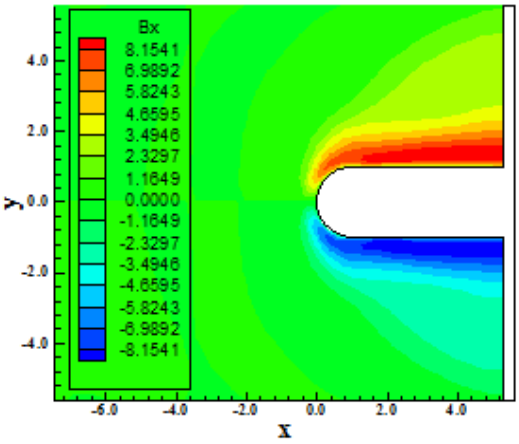

Fig. 53. B_x magnetic component contours (RK-YGO96).

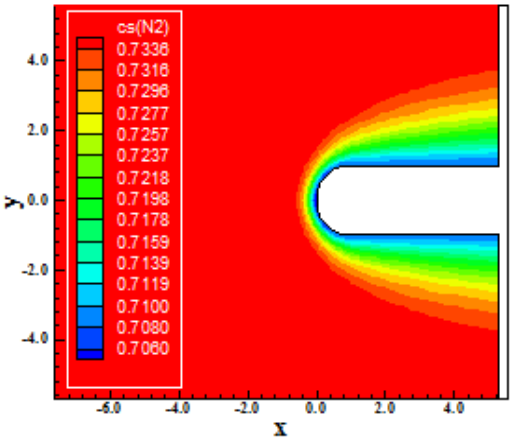

Fig. 54. N_2 mass fraction contours (RK-YGO96).

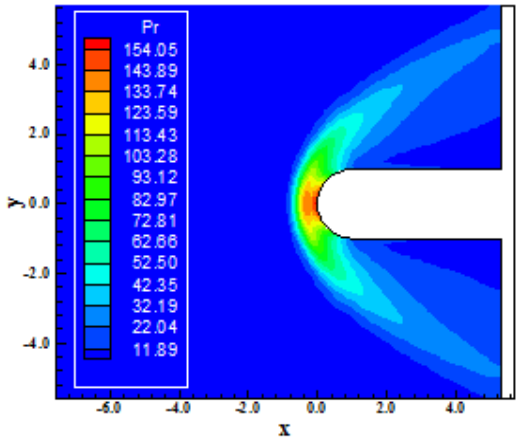

Fig. 55. Pressure contours (RK-C97).

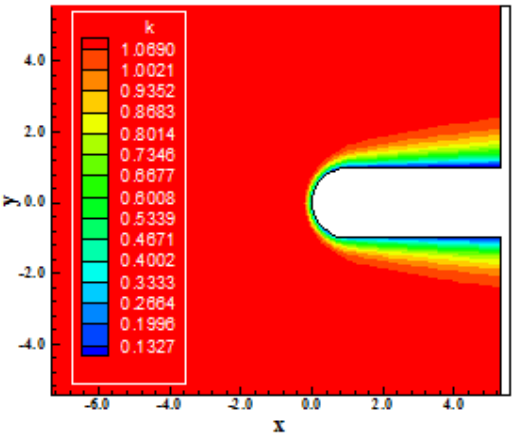

Fig. 56. Turbulent kinetic energy contours (RK-C97).

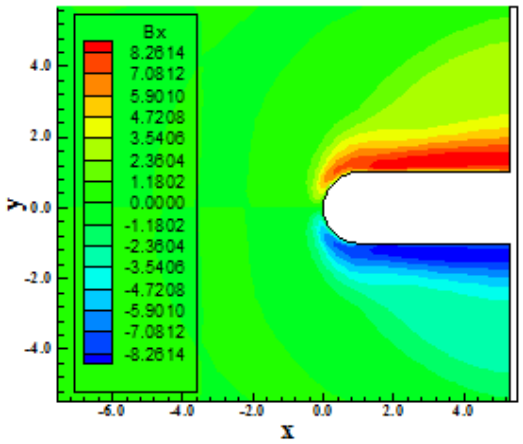

Fig. 57. B_x magnetic component contours (RK-C97).

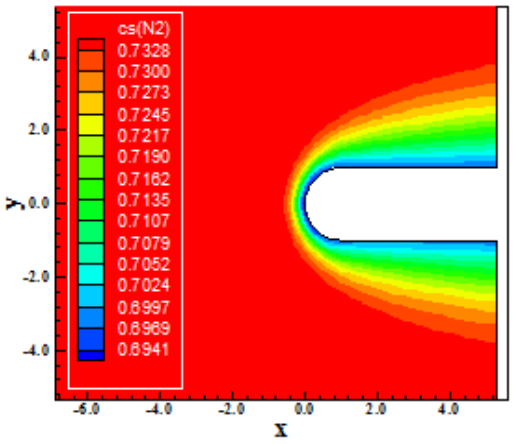

Fig. 58. N_2 mass fraction contours (RK-C97).

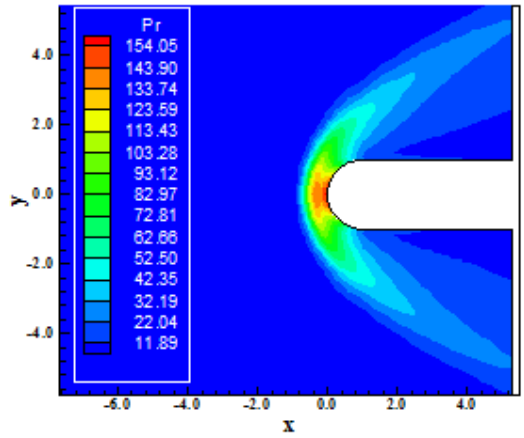

Fig. 59. Pressure contours (RK-RGYB98).

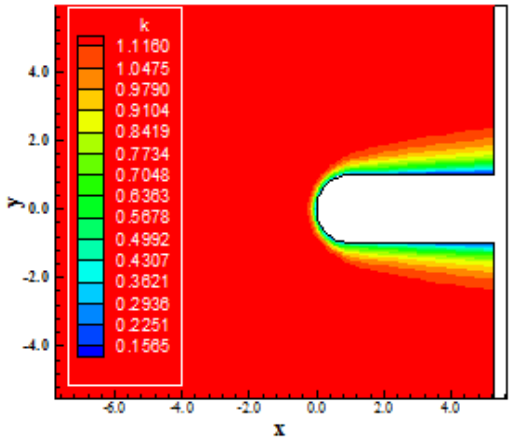

Fig. 60. Turbulent kinetic energy contours (RK-RGYB98).

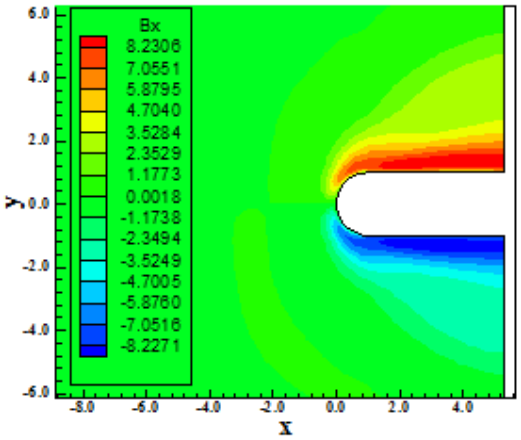

Fig. 61. B_x magnetic component contours (RK-RGYB98).

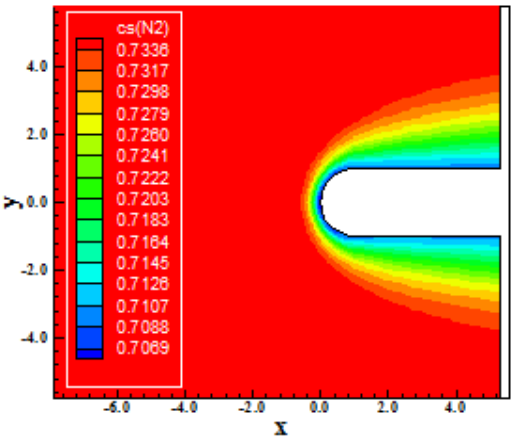

Fig. 62. N_2 mass fraction contours (RK-RGYB98).

Rumsey, Gatski, Ying and Bertelrud (1998) Results. Fig. 59 exhibits the pressure contours generated by the Maciel scheme as using the [17] turbulence model and the Runge-Kutta 4th order method to march in time. Good symmetry and homogeneous properties are observed. Fig. 60 shows the turbulent kinetic energy contours obtained by the Maciel scheme. Good levels of turbulence are obtained in agreement with the [13] and [16] solutions. Fig. 61 presents the B_x magnetic component contours obtained by the Maciel scheme as using the [17] turbulence model. Small differences are observed in quantitative terms, but in qualitative terms the resolution is good. Finally, Fig. 62 shows the N_2 mass fraction contours generated by the Maciel scheme as using the [17] turbulence model. Reasonable levels of dissociation are perceptible, but inferior to the other solutions.

Table 1. Values of S_x and S_y

Surface	S_x	S_y
i,j-1/2	$\left(y_{i+1,j} - y_{i,j}\right)$	$\left(x_{i,j} - x_{i+1,j}\right)$
i+1/2,j	$\left(y_{i+1,j+1} - y_{i+1,j}\right)$	$\left(x_{i+1,j} - x_{i+1,j+1}\right)$
i,j+1/2	$\left(y_{i,j+1} - y_{i+1,j+1}\right)$	$\left(x_{i+1,j+1} - x_{i,j+1}\right)$
i-1/2,j	$\left(y_{i,j} - y_{i,j+1}\right)$	$\left(x_{i,j+1} - x_{i,j}\right)$

10.4 Quantitative Analysis

In order to perform a quantitative analysis, the present reactive results are compared to the perfect gas solutions. The stagnation pressure at the blunt body nose was evaluated assuming the perfect gas formulation. Such parameter calculated at this way is not the best comparison, but in the absence of practical reactive results, this constitutes the best available solution.

Table 2. Initial conditions to the problem of the blunt body

Property	Value
$M_{initial}$	8.78
$\rho_{initial}$	0.00326 kg/m^3
$pr_{initial}$	687 Pa
$U_{initial}$	4,776 m/s
$T_{initial}$	694 K
$T_{v,initial}$	694 K
T_{REF}	0 K
Altitude	40,000 m
c_N	10^{-9}
c_O	0.07955
c_{O2}	0.13400
c_{NO}	0.05090
c_{NO+}	0.0
c_{e-}	0.0
L_{REF}	2.0 m
Re	2.3885x10^6
$k_{initial}$	10^{-6}
$\omega_{initial}$	$10U_{initial}/L_{REF}$
$Q_{h,initial}$	$10^{-4}\, h_{initial}^2$
$Q_{s,initial}$	$10^{-2}\sum_{i=1}^{ns} c_{i,initial}^2$
$B_{y,iinitial}$	0.15 T
$\mu_{M,\infty}$	1.2566x10^{-6} T.m/A
σ_∞	1,000 ohm/m

To calculate the stagnation pressure ahead of the blunt body, [46] presents in its B Appendix values of the normal shock wave properties ahead of the configuration. The ratio pr_0/pr_∞ is estimated as function of the normal Mach number and the stagnation pressure pr_0 can be determined from this parameter. Hence, to an initial Mach number of 8.78, the ratio pr_0/pr_∞ assumes the value 99.98. The value of pr_∞ is determined by the following expression:

$$pr_\infty = \frac{pr_{initial}}{\rho_\infty \times a_\infty^2}. \quad (123)$$

In the present study, $pr_{initial}$ = 687N/m^2, ρ_∞ = 0.004kg/m^3 and $a_\infty = a_{char}$ = 317.024m/s. Considering these values, one concludes that pr_∞ = 1.709 (non-dimensional). Using the ratio obtained from [46], the stagnation pressure ahead of the configuration nose is estimated as 170.87 unities. Table 3 compares the values of the stagnation pressure obtained from the simulations with this theoretical value and shows the percentage errors. As can be seen, the best results are provided by the [13], turbulence model, in all three time marching methods, with an error of 9.49%, inferior to 10.00%.

As the hypersonic flow along the present blunt body was simulated with a zero value to the attack angle, a zero lift coefficient is the expected value for this aerodynamic coefficient. Table 4 exhibits an analysis of the lift aerodynamic coefficient, based only on pressure contribution, in this study. As can be observed, the best value to the lift coefficient is obtained by the Maciel scheme when using the [13] turbulence model coupled with the Middle Point time marching method.

Table 3. Values of stagnation pressure and respective errors

March method:	Turbulence model:	Pr_0:	Error:
	Coakley (1983)	154.66	9.49
	Wilcox (1988)	154.06	9.84
Euler Backward	Yoder, Georgiadids and Orkwis (1996)	153.91	9.93
	Coakley (1997)	154.05	9.84
	Rumsey, Gatski, Ying and Bertelrud (1998)	154.12	9.80
	Coakley (1983)	154.66	9.49
	Wilcox (1988)	154.06	9.84
Middle Point	Yoder, Georgiadids and Orkwis (1996)	153.91	9.93
	Coakley (1997)	154.05	9.84
	Rumsey, Gatski, Ying and Bertelrud (1998)	154.12	9.80
	Coakley (1983)	154.66	9.49
	Wilcox (1988)	154.06	9.84
Runge-Kutta 4^{th}	Yoder, Georgiadids and Orkwis (1996)	153.89	9.94
	Coakley (1997)	154.05	9.84
	Rumsey, Gatski, Ying and Bertelrud (1998)	154.05	9.84

Table 4. Lift aerodynamic coefficient

March Method:	Turbulence Model:	c_L:
	Coakley (1983)	$1.9187x10^{-14}$
	Wilcox (1988)	$6.1555x10^{-10}$
Euler Backward	Yoder, Georgiadids and Orkwis (1996)	$3.8703x10^{-10}$
	Coakley (1997)	$1.7190x10^{-11}$
	Rumsey, Gatski, Ying and Bertelrud (1998)	$-3.7777x10^{-04}$
	Coakley (1983)	$1.4471x10^{-14}$
	Wilcox (1988)	$5.0839x10^{-11}$
Middle Point	Yoder, Georgiadids and Orkwis (1996)	$3.3753x10^{-10}$
	Coakley (1997)	$1.7189x10^{-11}$
	Rumsey, Gatski, Ying and Bertelrud (1998)	$-3.7767x10^{-04}$
	Coakley (1983)	$1.7918x10^{-14}$
	Wilcox (1988)	$6.1531x10^{-10}$
Runge-Kutta 4^{th}	Yoder, Georgiadids and Orkwis (1996)	$-1.3546x10^{-10}$
	Coakley (1997)	$-3.7747x10^{-11}$
	Rumsey, Gatski, Ying and Bertelrud (1998)	$-3.6983x10^{-04}$

Table 5. Computational data

March method:	Turbulence model:	CFL:	Iterations:
	Coakley (1983)	0.05	5,362
	Wilcox (1988)	0.05	5,452
Euler Backward	Yoder, Georgiadids and Orkwis (1996)	0.05	5,428
	Coakley (1997)	0.05	5,363
	Rumsey, Gatski, Ying and Bertelrud (1998)	0.05	5,363
	Coakley (1983)	0.05	5,359
	Wilcox (1988)	0.05	5,450
Middle Point	Yoder, Georgiadids and Orkwis (1996)	0.05	5,427
	Coakley (1997)	0.05	5,361
	Rumsey, Gatski, Ying and Bertelrud (1998)	0.05	5,361
	Coakley (1983)	0.05	5,362
	Wilcox (1988)	0.05	5,450
Runge-Kutta 4^{th}	Yoder, Georgiadids and Orkwis (1996)	0.03	9,058
	Coakley (1997)	0.05	5,364
	Rumsey, Gatski, Ying and Bertelrud (1998)	0.03	8,952

10.5 Computational Performance

Table 5 presents the computational data of the Maciel scheme for the blunt body problem. It shows the CFL number and the number of iterations to convergence for all studied cases in the current work. It can be verified that the best performance of the Maciel scheme occurred when using the [16] and [17] turbulence models coupled with the Middle Point time marching method.

As final conclusion, it is possible to highlight the [13] turbulence model as the best performance in estimating the stagnation pressure ahead of the blunt body. Moreover, the [16] and [17] turbulence models coupled with the Middle Point method were the most efficient in terms of computational effort. It is also important to note that all turbulence models predicted the stagnation pressure value with errors inferior to 10.00%.

11. CONCLUSIONS

In this work, a study involving magnetic field actuation over turbulent reentry flows in thermochemical non-equilibrium condition was performed. The Favre averaged Navier-Stokes equations coupled with the Maxwell equations, in conservative and finite volume contexts, employing structured spatial discretization, were studied. The numerical algorithm of Maciel was used to perform the reentry flow numerical experiments, which gave us an original contribution to the CFD community. Two types of numerical dissipation models were applied, namely: [41-42]. The “hot gas” hypersonic flow around a blunt body, in two-dimensions, was simulated. The convergence process was accelerated to steady state condition through a spatially variable time step procedure, which has proved effective gains in terms of computational acceleration [27-28]. Three time integration methods were tested to march the scheme in time, and it was another relevant contribution of the present work. They are: Euler Backward, Middle Point, and Runge-Kutta 4th order. The reactive simulations involved Earth atmosphere chemical model of seven species and eighteen reactions, based on the [29] model. The work of [25] was the reference one to present the fluid dynamics and Maxwell equations of electromagnetism based on a conservative and finite volume formalisms.

The results have indicated that the Maciel scheme, using the [41] artificial dissipation operator and the [13] turbulence model, yielded the best prediction of the stagnation pressure value with error inferior to 10.00%. Moreover, the best value to the lift aerodynamic coefficient was yielded by the Maciel scheme when using the [13] turbulence model coupled with the Middle Point time marching method. On the other hand, the [16] and [17] turbulence models coupled with the Middle Point method were the most efficient in terms of computational effort. This work was the couple of the [26] study, involving perfect gas magnetic actuation, [33-34] studies, involving reactive reentry flows, and [47], related to turbulent reactive flow, in two-dimensions.

In the present formulation, the Stokes hypothesis was adopted for defining the viscous tension even for a high speed flow (see [36]). This implementation is largely applied by the CFD community for high Mach number flows in all turbulence models that the authors have understanding and yields good results. Some references that use the Stokes hypothesis for high speed flow are [48-50].

The Maciel scheme was written in Fortran90 language and was developed in the Visual Studio 2008 environment and was only validated for reactive flows with magnetic actuation. For applications with reactive + magnetic + turbulence this is the first use of such method. For the reader interested only in the magnetic actuation with the Maciel scheme, some references are [51-53].

Finally, the validation and verification of the implemented code was performed by testing a benchmark physical problem (the blunt body) of the CFD community, where percentage errors were calculated in the evaluation of the stagnation pressure ahead of the geometry nose. The good results obtained demonstrated that the code was correctly implemented and that is capable to solve hypersonic flow problems, for what it was developed and applied.

ACKNOWLEDGEMENTS

The first author would like to thank the ITA facilities that allowed the realization of this work. He would also like to thank the CAPES by the financial support conceded under the form of a scholarship.

COMPETING INTERESTS

Authors have declared that no competing interests exist.

REFERENCES

1. Narayan JR, Girimaji SS. Turbulent reacting flow computations including turbulence-chemistry interactions. AIAA Paper 92-0342; 1992.
2. Gnoffo PA, Gupta RN, Shinn JL. Conservation equations and physical models for hypersonic flows in thermal and chemical nonequilibrium. NASA TP 2867; 1989.
3. Liu M, Vinokur M. Upwind algorithms for general thermo-chemical nonequilibrium flows. AIAA Paper 89-0201; 1989.
4. Park C. Radiation enhancement by nonequilibrium in Earth's atmosphere. Journal of Spacecraft and Rockets. 1985; 22(1): 27-36.
5. Park C. Problem of rate chemistry in the flight regimes of aeroassissted orbital transfer vehicles. Thermal design of aeroassissted orbital transfer vehicles, Progress in Astronautics and Aeronautics. Edited by H. F. Nelson, AIAA, NY. 1985; 96:511-537.
6. Gnoffo PA. Three-dimensional AOTV flowfields in chemical nonequilibrium. AIAA Paper 86-0230; 1986.
7. Li CP. Implicit methods for computing chemically reacting flow. NASA TM-58274; 1986.
8. Lee JH. Basic governing equations for the flight regimes of aeroassisted orbital transfer vehicles. Thermal design of aeroassisted transfer vehicles. Progress in Astronautics and Aeronautics. AIAA. 1985; 96:3-53.
9. Park C. Convergence of computation of chemically reacting flows. Thermophysical aspects of reentry flows. Progress in Astronautics and Aeronautics. Edited by J. N. Moss and C. D. Scott, AIAA, NY. 1986; 103:478-513.
10. Park C. Assessment of two-temperature kinetic model for dissociating and weakly-ionizing nitrogen. AIAA Paper 86-1347; 1986.
11. Park C. Calculation of nonequilibrium radiation in the flight regimes of aeroassissted orbital transfer vehicles. Thermal design of aeroassissted orbital transfer vehicles. Progress in Astronautics and Aeronautics. Edited by H. F. Nelson, AIAA, NY. 1985;96:395-418.
12. Park C. Nonequilibrium air radiation (NEQAIR) program: User's manual. NASA TM-86707; 1985.
13. Coakley TJ. Turbulence modeling methods for the compressible Navier-Stokes equations. AIAA Paper 83-1693; 1983.
14. Wilcox DC. Reassessment of the scale-determining equation for advanced turbulence models. AIAA Journal. 1988; 26(11):1299-1310.
15. Yoder DA, Georgiadids NJ, Orkwis PD. Implementation of a two-equation k-omega turbulence model in NPARC. AIAA Paper 96-0383; 1996.
16. Coakley TJ. Development of turbulence models for aerodynamic applications. AIAA Paper 97-2009; 1997.
17. Rumsey CL, Gatski TB, Ying SX, Bertelrud A. Prediction of high-lift flows using turbulent closure models. AIAA Journal. 1998;36(5):765-774.
18. Davidson PA. Magnetohydrodynamics in materials processing. Ann. Rev. Fluid Mech. 1999;31:273-300.
19. Ziemer RW, Bush WB. Magnetic field effects on bow shock stand-off distance. Physical Review Letters. 1958;1(2):58-59.
20. Meyer RX. Magnetohydrodynamics and aerodynamic heating. ARS Journal. 1959; 29(3):187-192.
21. Gurijanov EP, Harsha PT. AJAX: New Directions in Hypersonic Technology. AIAA Paper 96-4609; 1996.
22. Brichkin DI, Kuranov AL, Sheikin EG. MHD-technology for scramjet control. AIAA Paper 98-1642; 1998.
23. Ganiev YC, Gordeev VP, Krasilnikov AV, Lagutin VI, Otmennikov VN, Panasenko AV. Theoretical and experimental study of the possibility of reducing aerodynamic drag by employing plasma injection. AIAA Paper 99-0603; 1999.
24. Adamovich IV, Subramanian VV, Rich JW, Macheret SO. Phenomenological analysis of shock-wave propagation in weakly ionized plasmas. AIAA Journal. 1998; 36(5):816-822.
25. Gaitonde DV. Development of a solver for 3-D non-ideal magnetogasdynamics. AIAA Paper 99-3610; 1999.
26. Maciel ESG. Magnetic formulation and first-order schemes in 2D and 3D – Euler, Navier-Stokes and Maxwell equations in 2D and 3D – Perfect gas formulation. Saarbrücken, Deutschland: Lambert

Academic Publishing (LAP). 2015;Ch. 7: 225-290.

27. Maciel ESG. Simulations in 2D and 3D applying unstructured algorithms, Euler and Navier-Stokes equations – Perfect gas formulation. Saarbrücken, Deutschland: Lambert Academic Publishing (LAP). 2015; Ch. 1:26-47.
28. Maciel ESG. Simulations in 2D and 3D applying unstructured algorithms, Euler and Navier-Stokes equations – Perfect gas formulation. Saarbrücken, Deutschland: Lambert Academic Publishing (LAP). 2015; Ch. 6:160-181.
29. Blottner FG. Viscous shock layer at the stagnation point with nonequilibrium air chemistry. AIAA Journal. 1969;7(12): 2281-2288.
30. Narayan JR. Computation of compressible reacting flows using a two-equation turbulence model. 4th International Symposium on Computational Fluid Dynamics, Davis, California. September; 1991.
31. Williams FA. Combustion Theory. Addison-Wesley Publishing Company, Inc. Reading, MA. 1965;358-429.
32. Drummond JP, Carpenter MH, Riggins DW. Mixing and mixing enhancement in supersonic reacting flows. High Speed Propulsion Systems: Contributions to Thermodynamic Analysis. Ed. E. T. Curran and S. N. B. Murthy, American Institute of Astronautics and Aeronautics (AIAA), Washington, D. C.; 1990.
33. Maciel ESG. Hypersonic reactive flow simulations in two-dimensions, chemical and thermochemical non-equilibrium conditions. Saarbrücken. Deutschland: Lambert Academic Publishing (LAP). 2015; Ch. 5:333-406.
34. Maciel ESG. Hypersonic reactive flow simulations in two-dimensions, chemical and thermochemical non-equilibrium conditions. Saarbrücken. Deutschland: Lambert Academic Publishing (LAP). 2015; Ch. 6:407-490.
35. Favre A. Statistical equations of turbulent gases. Institut de Mechanique Statistique de la Turbulence, Marseille.
36. Maciel ESG, and Andrade CR. Turbulent thermochemical non-equilibrium reentry flows in 2D - Eleven species. Asian Journal of Mathematics and Computer Research. 2017;20(4):179-217.
37. Prabhu RK. An implementation of a chemical and thermal nonequilibrium flow solver on unstructured meshes and application to blunt bodies. NASA CR-194967; 1994.
38. Saxena SK, Nair MT. An improved Roe scheme for real gas flow. AIAA Paper 2005-587; 2005.
39. Ait-Ali-Yahia D, Habashi WG. Finite element adaptive method for hypersonic thermochemical nonequilibrium flows. AIAA Journal. 1997;35(8):1294-1302.
40. Long LN, Khan MMS, Sharp HT. Massively parallel three-dimensional Euler / Navier-Stokes method. AIAA Journal. 1991;29(5): 657-666.
41. Mavriplis DJ. Accurate multigrid solution of the Euler equations on unstructured and adaptive meshes. AIAA Journal. 1990; 28(2):213-221.
42. Turkel E, Vatsa VN. Effect of artificial viscosity on three-dimensional flow solutions. AIAA Journal. 1994;32(1):39-45.
43. Vincent WG, Kruger Jr. CH. Introduction to physical gas dynamics. Malabar, Florida, EUA: Krieger Publishing Company. 2002; Ch. 1:1-26.
44. Fox RW, McDonald AT. Introdução à mecânica dos fluidos. Guanabara Editor; 1988.
45. Maciel ESG. Simulação numérica de escoamentos supersônicos e hipersônicos utilizando técnicas de dinâmica dos fluidos computacional. Doctoral Thesis, ITA, CTA, São José dos Campos, SP, Brazil; 2002.
46. Anderson Jr. JD. Fundamentals of aerodynamics. McGraw-Hill, Inc., 5th Edition. 2010;1008.
47. Maciel ESG. Turbulent thermochemical non-equilibrium reentry flows in 2D. Computational and Applied Mathematics Journal. 2015;1(4):201-224.
48. Warren ES, Harris JE, Hassan HA. A transition model for high speed flow. AIAA Paper 94-1851-CP; 1994.
49. Abid R, Speziale CG, Thangam S. Application of a new k-τ model to near wall turbulent flows. AIAA Paper 91-0614; 1991.
50. Olsen ME, Lillard RP, Coakley TJ. The lag model applied to high speed flows. NASA Technical Report NAS 05-005; 2005.
51. Maciel ESG. Magnetic field applied to thermochemical non-equilibrium reentry flows in 2D - Five species. International Journal of Computational Fluid Dynamics. 2015;1(11):1-24.

52. Maciel ESG, Andrade CR. Magnetic field applied to thermochemical non-equilibrium reentry flows in 2D - Seven species", International Journal of Applied Physics. 2016;6(2):117-172.

53. Maciel ESG. Magnetic field in reentry flows in 2D: Eleven species. Journal of Advances in Mathematics and Computer Science. 2017;24(6):1-36.

© 2017 Maciel and Andrade; This is an Open Access article distributed under the terms of the Creative Commons Attribution License (http://creativecommons.org/licenses/by/4.0), which permits unrestricted use, distribution, and reproduction in any medium, provided the original work is properly cited.

Peer-review history:
The peer review history for this paper can be accessed here:
http://sciencedomain.org/review-history/21729